JOURNAL OF GEOPHYSICAL RESEARCH, VOL. 93, NO. B8, PAGES 9093–9112, AUGUST 10, 1988

Microearthquakes Beneath Median Valley of Mid-Atlantic Ridge Near 23°N: Tomography and Tectonics

DOUGLAS R. TOOMEY[1]

MIT/WHOI Joint Program in Oceanography, Woods Hole Oceanographic Institution, Woods Hole, Massachusetts

SEAN C. SOLOMON

Department of Earth, Atmospheric, and Planetary Sciences, Massachusetts Institute of Technology, Cambridge

G. M. PURDY

Department of Geology and Geophysics, Woods Hole Oceanographic Institution, Woods Hole, Massachusetts

Data from a microearthquake experiment in the median valley of the Mid-Atlantic Ridge near 23°N in 1982 are used to measure earthquake source parameters, to determine the laterally heterogeneous seismic velocity structure across the inner floor, and to develop a kinematic tectonic model for this portion of the median valley. Fifty-three microearthquakes occurred over a 10-day period beneath the median valley inner floor and eastern rift mountains. Twenty of 23 well-located inner floor epicenters define a line of activity, about 17 km long, having a strike of N25°E and located near an along-axis depression some 300–400 m deeper than surrounding regions. Earthquakes with well-resolved hypocenters generally have focal depths of 4–8 km beneath the seafloor of both the inner floor and the rift mountains; the hypocentral locations are robust with respect to plausible lateral variations in seismic velocity structure. Composite fault plane solutions for inner floor events indicate normal faulting on planes dipping at angles near 45°. Normal faulting mechanisms, although poorly constrained, are also indicated for the rift mountain microearthquakes. Seismic moments, approximate fault dimensions, and average stress drops for the largest events recorded are 10^{19}–10^{20} dyn cm, 200–400 m, and 1–70 bars, respectively. A two-dimensional tomographic inversion of *P* wave travel time residuals from microearthquakes and local shots indicates a well-resolved lateral heterogeneity in crustal velocity structure across the median valley inner floor. *P* wave velocities at 1–5 km depth within a zone less than 10 km wide beneath the central inner floor are lower by several percent than in surrounding regions. The most likely explanation for the low velocities is that the region is the site of the most recent local magmatic injection and remains pervasively fractured as a result of rapid hydrothermal quenching of the newly emplaced crustal column. By this view, the seismic velocity structure at the ridge axis evolves, probably by the sealing of cracks and pores, within the first few hundred thousand years of crustal accretion. Consideration of the detailed Sea Beam bathymetry in this region of the inner floor, the characteristics of large earthquakes that the region has experienced during the past 25 years, and the results of the microearthquake and tomography analysis suggests that this section of the median valley has been undergoing continued horizontal extension and block faulting without significant crustal injection of magma for at least the past 10^4 years.

INTRODUCTION

The physical processes controlling crustal accretion at a mid-ocean ridge are known to display strong spatial and temporal variations. The nature and distribution of earthquakes and the lateral heterogeneity of seismic velocity structure constitute two crucial types of information on the current state of any given ridge segment. In 1982 two complementary seismic experiments were carried out to obtain such information for the segment of the median valley of the Mid-Atlantic Ridge south of its intersection with the Kane Fracture Zone (Figure 1). A seismic refraction experiment utilizing explosive charges and ocean bottom hydrophones (OBHs) was conducted along the median valley to a distance of 120 km south of the ridge-transform intersection; the analysis and interpretation of the data in terms of crustal structure and its along-axis variation have been described by *Purdy and Detrick* [1986]. A microearthquake experiment was carried out in the median valley near 22°45′N with a network of seven OBHs and two ocean bottom seismometers (OBSs); the hypocenters and fault plane solutions of 26 microearthquakes located beneath the inner floor and rift mountains were reported by *Toomey et al.* [1985] (hereinafter referred to as paper 1). In this paper we present additional data from the microearthquake experiment on the nature of seismic faulting in the area and on the lateral variation in crustal *P* wave velocity structure across the median valley; from these results and those of other studies of the region we develop a simple model for the recent tectonic evolution of this segment of the median valley.

The segment of the Mid-Atlantic Ridge south of the Kane Fracture Zone has been the focus since 1982 of several additional geological and geophysical investigations, including a Sea Beam bathymetric survey [*Detrick et al.*, 1984], a Sea MARC I side scan sonar imaging survey [*Mayer et al.*, 1985], an investigation of the mechanisms of several large median

[1]Now at Department of Earth, Atmospheric and Planetary Sciences, Massachusetts Institute of Technology, Cambridge.

Paper number 7B5057.
0148-0227/88/007B-5057$05.00

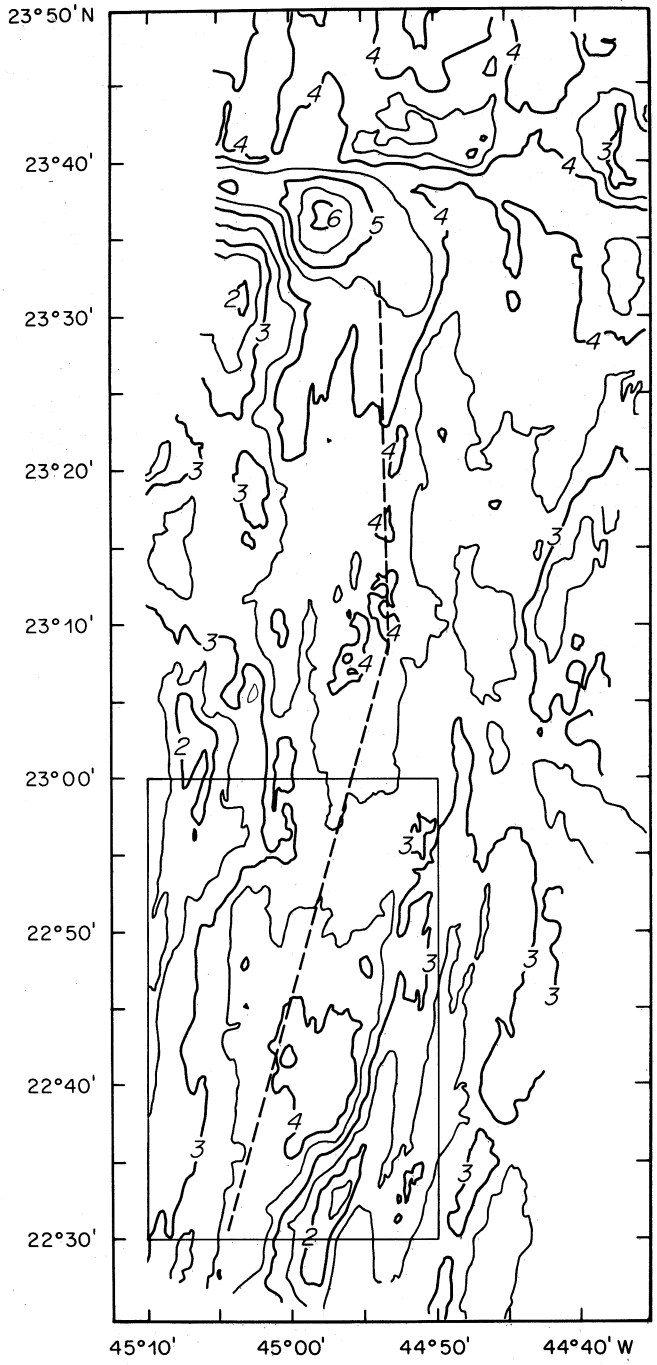

Fig. 1. Bathymetry of the Mid-Atlantic Ridge median valley to the south of the Kane Fracture Zone (0.5-km contour interval) [from *Detrick et al.*, 1984]. The rectangle in the southern portion of the figure defines the area of the 1982 microearthquake survey that is shown in detail in Figure 2. The dashed line shows the location of the refraction line used to determine the crustal structure along the axis of the median valley [*Purdy and Detrick*, 1986].

valley earthquakes [*Huang et al.*, 1986], discovery of a hydrothermal vent field [*Kong et al.*, 1985; *Ocean Drilling Program Leg 106 Scientific Party*, 1986], crustal drilling at two axial sites [*Ocean Drilling Program Leg 109 Scientific Party*, 1986], and geological exploration by submersible along several traverses of the median valley [*Karson et al.*, 1987]. Overall, these investigations document significant along-axis variability in median valley morphology, volcanic and hydrothermal activity, and styles of tectonic extension. The diverse observations of this segment of the Mid-Atlantic Ridge median valley allow us to place the results of the microearthquake and seismic velocity studies within the context of a well-documented regional description of axial processes.

We begin by augmenting the number of located microearthquakes by a factor of 2 from that considered earlier (paper 1). The additional data help to define both seismicity patterns and possible fault geometries. We also estimate seismic moments and approximate source dimensions for the best located earthquakes. We then employ a tomographic technique [*Thurber*, 1983] to invert the *P* wave travel time residuals from microearthquakes and local shots to obtain a two-dimensional representation of crustal structure across the median valley inner floor. We show that the travel time residual data can resolve a region of relatively low *P* wave velocities at 1–5 km depth beneath the central inner floor, probably the site of most recent crustal accretion. On the basis of several synthetic experiments we demonstrate that neither this lateral heterogeneity in structure beneath the inner floor nor the velocity heterogeneity associated with the variation in topography across the transition from inner floor to rift mountains should contribute significant bias to microearthquake locations. Finally, we synthesize the microearthquake and crustal structure information with the bathymetry [*Detrick et al.*, 1984] and the record of larger earthquakes [*Huang et al.*, 1986] to suggest that this section of median valley has been undergoing continued horizontal extension and modest block rotation without crustal level magma injection for at least the last 10^4 years.

MICROEARTHQUAKE DATA

In paper 1, consideration was limited to microearthquakes with five or more arrival time readings, including at least one *S* wave arrival time obtained from a three-component OBS. These criteria were satisfied by 26 microearthquakes, a small fraction of the several hundred events recorded during the experiment. An expanded microearthquake population is considered in this paper by relaxing the criteria on the number and type of arrival times to include all events with at least four arrival times. The locations of the smaller events added to the expanded data set are not, in general, as accurate as those of paper 1, but similarity in waveform and relative arrival time to larger and better recorded events can nonetheless give further confidence in the locations. The additional information obtained from the enlarged data set provides an improved insight into the tectonic processes active along this segment of the median valley.

The acoustically relocated instrument positions, hypocenter location procedure, and assumed seismic velocity model are as in paper 1. In a later section we assess the effects of lateral heterogeneity of seismic velocity on hypocentral locations, and we confirm the accuracy of the locations obtained on the assumption of lateral homogeneity. Figure 2 shows the configuration of the instrument network in the context of the detailed bathymetry of the median valley [*Detrick et al.*, 1984].

HYPOCENTER LOCATIONS

An additional 27 microearthquakes have been located beyond those presented in paper 1; their hypocentral parameters are given in Table 1. Twenty-four of the 27 new events were located with four or more *P* wave arrival times but no *S* wave arrival times, while the remaining three events were lo-

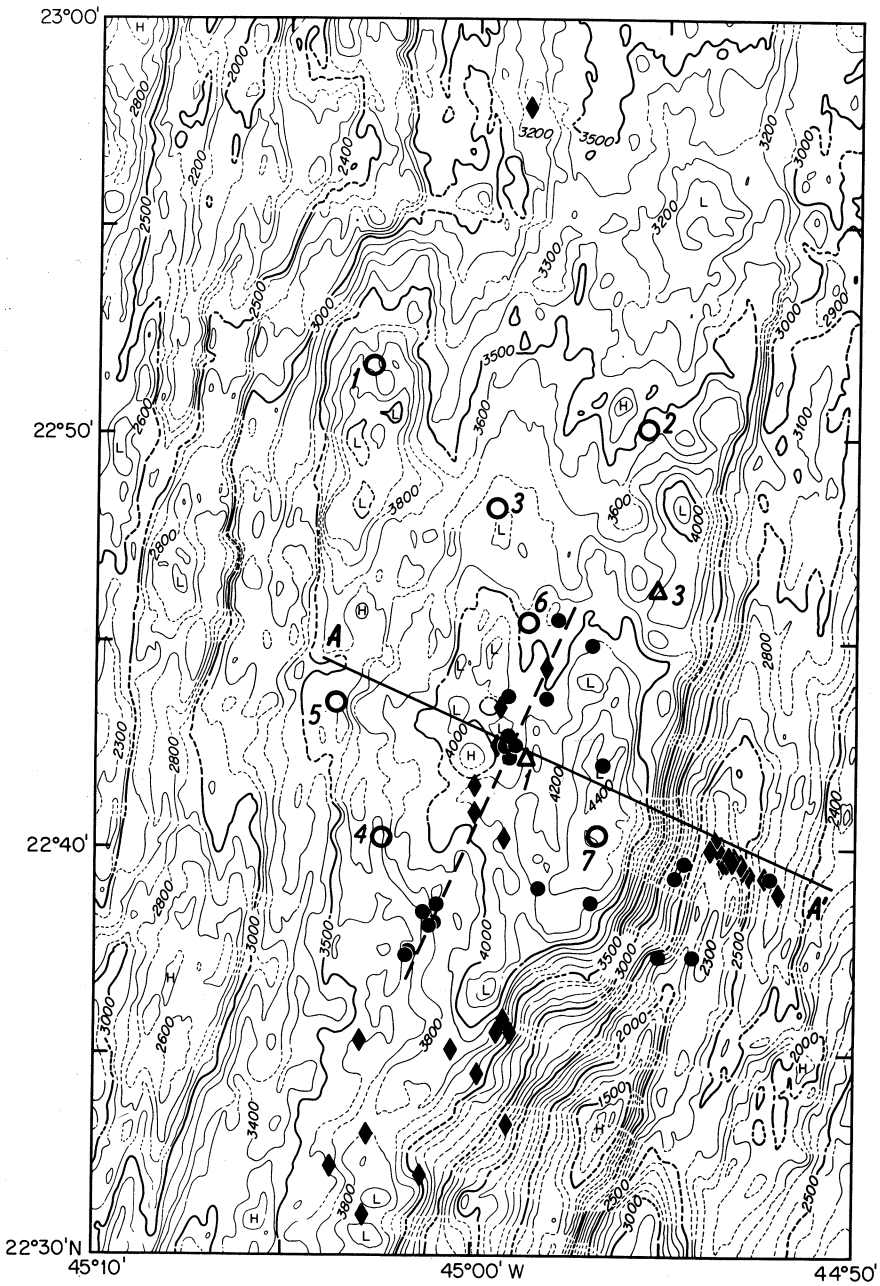

Fig. 2. Configuration and setting of the microearthquake experiment. Open symbols denote seismic instruments: circles are Woods Hole Oceanographic Institution OBHs, triangles are Massachusetts Institute of Technology OBSs. Solid symbols indicate microearthquake epicenters: circles denote epicenters with independently resolved focal depth, and diamonds denote epicenters determined for a fixed focal depth. Bathymetric contours, at 100-m intervals, are from the Sea Beam survey of *Detrick et al.* [1984]; closed highs and lows are indicated by H and L, respectively. Contours are dashed in regions between Sea Beam swaths. The solid line AA′ marks the location of the vertical cross section depicted in Figure 3. The dashed line through the epicenters in the inner floor strikes at N25°E.

cated with three *P* arrival times and one *S* time. The statistical uncertainty of these 27 locations are, in general, larger than the errors reported for hypocentral locations in paper 1, a result of inadequate observations that cause the inverse problem to be ill conditioned. The smallest eigenvalue in the singular value decomposition of the partial derivative matrix [*Klein*, 1978] is usually associated with an eigenvector whose predominant component is the focal depth. When this eigenvalue is less than a cutoff value [*Klein*, 1978], we fix the focal depth and estimate epicenter and orgin time; these events are designated by the term "poor depth control" (pdc) in Table 1. In the final inversion iteration for some of these events an additional eigenvalue associated with one of the epicentral coordinates was also less than the cutoff value; for these events an epicentral uncertainty of 5 km was arbitrarily assigned (Table 1). For the 27 events in Table 1 the overall rms travel time residual is 0.05 s; excluding two events located more than 10 km south of the array, the overall rms residual is 0.03 s. An unbiased estimate of the sample standard deviation of travel times for an individual event in Table 1 would be approximately twice the rms residual, taking into account the number of degrees of freedom. Such an estimate, however, ignores the statistical contraints on data uncertainty provided by the better recorded events reported in paper 1. Under the

TABLE 1. New Hypocentral Parameters of Microearthquakes Beneath the Mid-Atlantic Ridge Near 23°N

Origin Time		Latitude,	Longitude,	Depth,	Number of Readings		mag,	dcs,	rms,	erh,	erz,
Date	Time, UT	N	W	km	*P*	*S*	deg	km	s	km	km
Feb. 22	2246:22.11	22°35.2′	45°03.0′	6	4	0	308	9.4	0.12	5	pdc
Feb. 24	0107:53.05	22°44.3′	44°58.1′	6	4	0	183	2.3	0.02	0.7	pdc
Feb. 24	0401:18.93	22°35.7′	44°59.2′	5	4	0	301	9.4	0.06	5	pdc
Feb. 24	0734:00.91	22°40.8′	45°00.0′	6	4	0	158	4.3	0.07	0.7	pdc
Feb. 24	0757:18.75	22°43.7′	44°59.1′	5.7	5	0	132	3.4	0.02	0.6	1.6
Feb. 24	0907:46.11	22°39.6′	44°53.0′	5	5	0	309	6.7	0.03	5	pdc
Feb. 24	1055:24.15	22°40.1′	44°53.6′	5	4	0	305	5.3	0.02	5	pdc
Feb. 24	2154:50.66	22°39.7′	44°53.3′	5	5	0	307	6.1	0.02	5	pdc
Feb. 24	2223:45.32	22°39.9′	44°53.8′	5	4	0	305	5.2	0.03	5	pdc
Feb. 25	0205:38.24	22°39.2′	44°52.3′	5	5	0	313	7.9	0.03	4.6	pdc
Feb. 25	0206:16.93	22°39.6′	44°53.2′	5	5	0	308	6.2	0.03	5	pdc
Feb. 25	0323:36.10	22°39.4′	44°52.9′	5	4	0	310	6.8	0.02	5	pdc
Feb. 25	0533:49.74	22°39.4′	44°52.7′	5	5	0	310	7.1	0.03	5	pdc
Feb. 25	0621:56.93	22°45.6′	44°57.9′	4.5	4	0	247	1.4	0.00	2.4	1.1
Feb. 25	0806:18.83	22°39.6′	44°53.3′	5	4	0	308	6.0	0.01	5	pdc
Feb. 25	0808:36.77	22°39.6′	44°53.4′	5	5	0	307	5.9	0.01	5	pdc
Feb. 25	0812:27.81	22°39.6′	44°53.1′	5	5	0	307	6.3	0.03	5	pdc
Feb. 25	0823:56.60	22°38.8′	44°52.0′	5	4	0	315	8.7	0.01	4.6	pdc
Feb. 25	2106:44.19	22°42.8′	44°59.2′	6.3	5	0	128	5.1	0.03	0.6	1.9
Feb. 26	0014:07.00	22°39.8′	44°53.5′	5	4	0	308	5.7	0.02	5	pdc
Feb. 26	0049:49.63	22°30.9′	45°02.8′	6	5	0	326	17.2	0.16	5	pdc
Feb. 26	1825:49.73	22°44.9′	44°56.9′	4.5	5	0	212	3.0	0.01	1.0	1.0
Feb. 26	2041:53.42	22°35.4′	44°59.0′	5	4	0	304	9.8	0.04	5	pdc
March 1	1103:34.05	22°43.3′	44°59.3′	6	4	0	124	4.1	0.01	0.6	pdc
March 3	2127:18.13	22°41.4′	45°00.0′	6	3	1	191	2.7	0.03	1.5	pdc
March 4	0636:19.46	22°42.5′	44°59.5′	6	3	1	183	1.5	0.04	2.7	pdc
March 4	1015:35.75	22°40.2′	44°59.3′	6	3	1	223	3.9	0.03	1.2	pdc

Definitions are as follows: mag, maximum azimuthal gap; dcs, distance to the closest station; rms, root-mean-square travel time residual; erh, horizontal error at 95% confidence (from projection of error ellipse onto horizontal plane); erz, error in depth at 95% confidence; pdc, poor depth control. Values of depth and erh given only to one significant figure are fixed estimates; see text.

assumption that the sources of statistical uncertainty are stationary throughout the deployment, the uncertainty in travel time estimated from the full data set [*Jordan and Sverdrup*, 1981] is 0.04 s, a value consistent with our assumed "picking error" (paper 1). This estimate of travel time uncertainty is used to calculate the formal errors given in Table 1.

Of the total of 53 microearthquakes in paper 1 and Table 1, 22 have epicentral coordinates and focal depths which may be independently estimated. Tests conducted with various plane-layered velocity models indicate that the hypocentral parameters of these well-recorded events are not sensitive to uncertainties in the average *P* or *S* wave velocity structure (paper 1). Focal depth for the remaining 31 events is poorly resolved, either because the epicenter lies more than 10 km from the nearest instrument of because the number of reliable arrival times is too small. For 16 of the events, epicentral coordinates can nonetheless be resolved when focal depth is held to a fixed value.

The epicenters of all 53 microearthquakes from paper 1 and Table 1 are shown in Figure 2. Microearthquake activity during the deployment period was limited to the inner floor of the median valley and to the eastern rift mountains. No earthquakes detected during the deployment period had a location in the western rift mountains, and only one event occurred north of about latitude 22°45′N. On the basis of the 26 events in paper 1 the microearthquake activity had been grouped into four geographic regions. Two of these regions were located on the inner floor, including one within the monitoring array and one 5–6 km south of the array. With the additional data in this paper it is evident that the inner floor activity cannot be divided into distinct regions. We therefore divide our discussion of microearthquake activity into three categories: earthquakes beneath the inner floor, earthquakes beneath the eastern rift mountains, and events distant from the network with poorly constrained epicenters.

Seismicity of the Median Valley Inner Floor

The new data set in Table 1 includes 10 events beneath the inner floor, four with well-resolved focal depths and six with epicenters estimated after fixing the depth. For the latter six microearthquakes, epicenters were calculated at a series of fixed focal depths from 1 to 20 km. On the basis of the rms travel time residual as a function of assumed focal depth and the predominance of focal depths in the range 5–8 km for the better recorded inner floor microearthquakes, a fixed focal depth of 6 km was selected for the estimation of epicentral coordinates. The range in epicentral locations for other values of depth in the range 5–8 km suggest that the formal errors listed in Table 1 for these six epicenters should be increased by factors of 2–4.

Combining the new locations with those previously reported (paper 1) yields a total of 23 microearthquakes beneath the inner floor of the median valley during the 10-day deployment period of the full network; for 17 of these events, epicenters and focal depths may be independently resolved. The formal errors in hypocentral coordinates of the better located microearthquakes beneath the inner floor are approximately ± 1 km at the 95% confidence level (paper 1). Twenty of the 23 epicenters within the inner floor occur within approximately 1 km of a line which strikes N25°E (Figure 2). During the de-

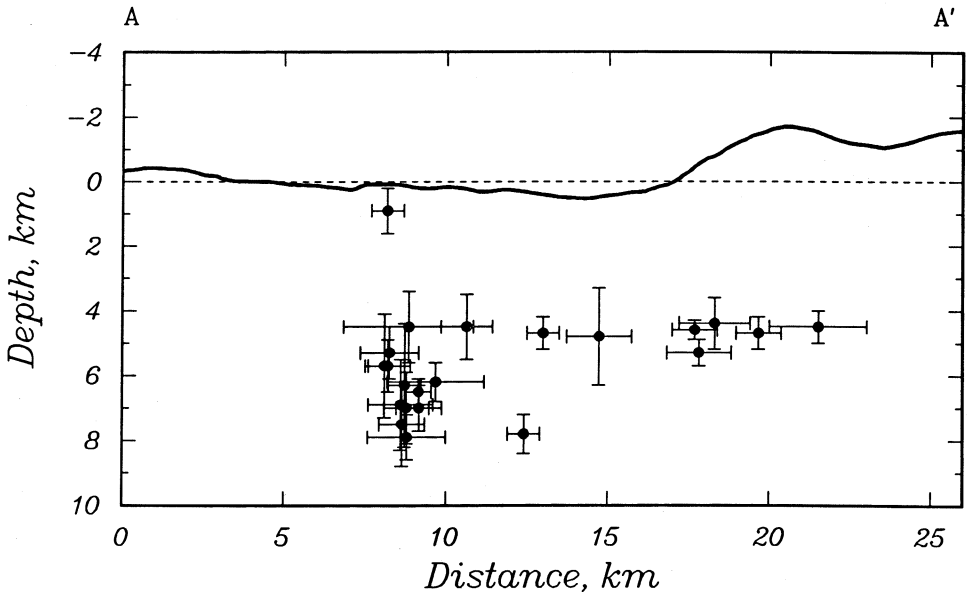

Fig. 3. Well-resolved focal depths of microearthquakes beneath the median valley. Hypocenters have been projected onto the vertical plane through profile AA′ (Figure 2). Error bars show 95% confidence limits for focal depth and horizontal location in the plane of the figure. All depths are relative to the datum indicated by the dashed line. There is no vertical exaggeration of the bathymetry.

ployment period, seismic activity was observed along this line over a distance of about 17 km. For comparison, the regional trend of the median valley between latitudes 22°30′ and 23°N is about N10°–15°E, and the azimuth of a great circle between the deployment site and the spreading pole between the North American and African plates is N10°E [*Minster and Jordan*, 1978]. The hypocenters of the 17 events with well-resolved focal depths are projected onto a vertical plane that is perpendicular to the N25°E trend of seismicity in Figure 3. As documented in paper 1, most microearthquakes beneath the inner floor have focal depths between 5 and 8 km. For comparison, *Purdy and Detrick* [1986] estimated that the crust-mantle transition beneath the inner floor at this site occurs at approximately 6–7 km depth.

Seismicity of the Inner Rift Mountains

The newly located microearthquakes in Table 1 include 13 events beneath the eastern rift mountains. None of these 13 microearthquakes were sufficiently well recorded to constrain focal depth. For two of the events the epicenters were determined with focal depth held fixed at 5 km. For the remaining 11 the epicenters are not well constrained by travel time analysis alone, but a comparison of seismic waveforms with those from the two events with resolvable epicenters helps to estimate epicentral coordinates. Figure 4 shows the seismograms recorded by OBH 7 (Figure 2) from these 13 events. All but one of the events in Figure 4 occurred during a single 24-hour period. Seismograms from the first 11 events in Figure 4 display a remarkable degree of similarity. The correlation coefficient between the records of events 1 and 2 is 0.84; similar values are obtained for different combinations of the first 11 waveforms. The repeatability of short-period waveforms from these events implies that their source locations and mechanisms are nearly identical. There is also a strong similarity between the group of waveforms of the first 11 events in Figure 4 and those from the next two for which epicentral locations have been determined with more confidence. Probably all of these earthquakes occurred near the epicenters of the latter two earthquakes, toward the eastern end of the elongated zone of rift mountain activity indicated in Figure 2.

For all of the waveforms in Figure 4 there is a prominent phase arriving about 0.7 s after the initial *P* wave. This phase cannot be a direct *S* wave (converted at the seafloor), which should arrive 1.2 s after *P*. An examination of other hydrophone and seismometer records from these and other events has also led us to rule out the likelihood that this arrival

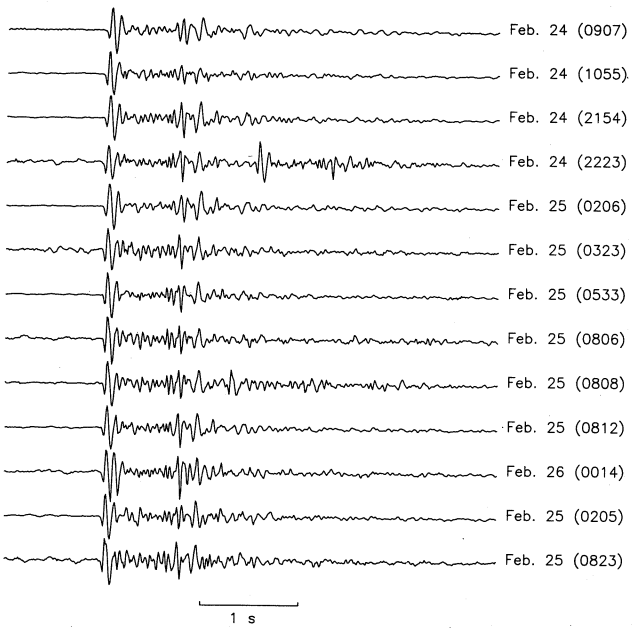

Fig. 4. Seismograms of 13 rift mountain earthquakes recorded by OBH 7. The first 11 events have epicentral coordinates and focal depth poorly resolved by travel times, while the last two events have well-resolved epicenters if the focal depth is held fixed. Seismograms are aligned at the *P* wave onset and are scaled to have identical maximum amplitudes.

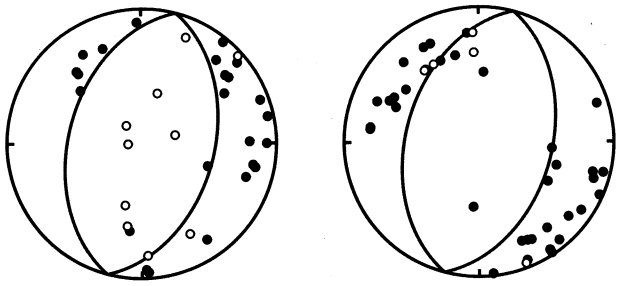

Fig. 5. Composite fault plane solutions of selected microearthquake. (*a*) Composite for seven inner floor events with epicenters within the network (February 24, 0757 UT; February 25, 0621 UT; February 25, 2106 UT; February 26, 1825 UT; February 26, 2224 UT; February 28, 2333 UT; and March 3, 1435 UT). (*b*) Composite for seven rift mountain events (February 24, 2151 UT; February 26, 0349 UT; March 2, 0825 UT; March 2, 1023 UT; March 3, 1611 UT; March 3, 1715 UT; and March 4, 0447 UT). Compressional arrivals are shown as solid circles, dilatations as open circles. Equal-area projections are of the lower focal hemisphere. Fault planes shown have strike and dip angles of (N15°E, 45°E) and (N15°E, 45°W).

corresponds to a multiple generated beneath the receiving station, a reflection from a near-source discontinuity, an arrival from a later travel time branch, or a complexity to the source time function. The phase was most prominent on OBH 7 and OBS 3, the two instruments nearest the steep scarps of the eastern rift mountains (Figure 2). The arrival time is consistent with that of a *P* wave that exited the seafloor along the inner wall, about 1 km to the east of the instruments, and traveled the final distance through the water. An *S* to *P* conversion at some interface along the path between the source and receiver is another possibility. We do not have sufficient information to test these suggestions further.

Including the events reported in paper 1, 18 microearthquakes can be located beneath the eastern rift mountains. The hypocenters of five rift mountain earthquakes with well-resolved focal depths, all from paper 1, are depicted on the vertical cross section in Figure 3. In paper 1 it was noted that uncertainty in these rift mountain hypocentral locations have an unknown contribution from the likely failure of the assumption of laterally homogeneous velocity structure used in hypocentral location. We address this question at length in a later section.

FOCAL MECHANISMS

First-motion polarities from the additional microearthquake data of this paper provide stronger constraints on composite focal mechanisms of the type presented in paper 1. A composite fault plane solution for seven inner floor events with epicenters within the network and independently resolved hypocentral parameters is depicted in Figure 5*a*. A composite focal mechanism from five inner floor events located to the south of the network was given in paper 1. First motions from an additional three well-located inner floor events were examined but were not included because of unusual hypocentral locations or apparently different source mechanisms. The composite first motions in Figure 5*a* clearly indicate a normal faulting mechanism. The two nodal planes dip at angles of about 45°, and both strike at approximately N15°E. Slip on a subhorizontal fault [cf. *Lilwall*, 1980] can be excluded for these events.

A composite fault plane solution of seven rift mountain earthquakes with well-resolved hypocenters is shown in Figure 5*b*. Only weak constraints are possible on the fault plane solution because of the comparatively poor coverage of the focal sphere. About all we may conclude is that most of these data are compatible with normal faulting.

SEISMIC MOMENTS AND SOURCE DIMENSIONS

Displacement spectra of *P* and *S* waveforms on OBS records and pressure spectra of *P* waveforms on OBH records were determined to estimate seismic moment and source dimensions of selected earthquakes. For an OBS, displacement spectra provide a valid measure of source properties only for a seismometer package that is well coupled to the seafloor [e.g., *Sutton et al.*, 1981; *Tréhu and Solomon*, 1981, 1983]. In our experiment, spectra on OBS 3 (Figure 2) appear uncontaminated by coupling resonance, but seismograms recorded on OBS 1 show an apparent resonance at 4–5 Hz in the waveform following the *S* arrival (Figure 4 in paper 1). Inspection of displacement spectra from OBS 1 confirm that *P* and *S* waveforms were complicated by coupling resonances. From *P* wave particle motions and incident angles we suggested in paper 1 that the OBS 1 seismometer package may have been resting on a slope inclined at 25°; such a steep slope may have contributed to the poorer coupling characteristics. Only spectra from OBS 3 were used to estimate seismic moment and corner frequency. Displacement spectra were determined from *P* and *S* waveforms recorded on the vertical component; corrections for instrument response and for attenuation followed *Tréhu and Solomon* [1983].

We determined the pressure spectra from *P* waves recorded on OBH 7, an instrument which yielded clear records of all but two of the events located beneath the inner floor and the eastern rift mountains. Spectra were corrected for instrument response [*Koelsch and Purdy*, 1979] and were converted to equivalent displacement spectra by dividing by $\rho c\omega$, where ω is the angular frequency and ρ and c are the density and sound speed of seawater, respectively. This correction is equivalent to the assumption that the *P* waves are incident as plane waves [*Urick*, 1975]. Displacement spectra calculated in this manner correspond to the modulus of the water particle displacement vector, so that an additional factor is required to give the vertical component of displacement. *P* wave spectra from the OBH were corrected for attenuation in the same manner as for the OBS. Examples of waveforms and displacement spectra from OBS 3 and OBH 7 are shown in Figure 6.

The seismic moment was estimated from the displacement spectral amplitude Ω_0 at low frequency using the formula of *Brune* [1970]:

$$M_0 = \frac{4\pi\rho_0 x V^3 \Omega_0}{KR} \tag{1}$$

where ρ_0 and V are the density and seismic velocity, respectively, at the source, x is the path length, R is a radiation pattern factor, and K is a correction for the interaction of seismic waves with the seafloor. The above formula holds for both *P* and *S* waves [*Hanks and Wyss*, 1972], provided that V, Ω_0, K, and R take on appropriate values for either *P* or *S* waves. For events beneath the rift mountains the focal mecha-

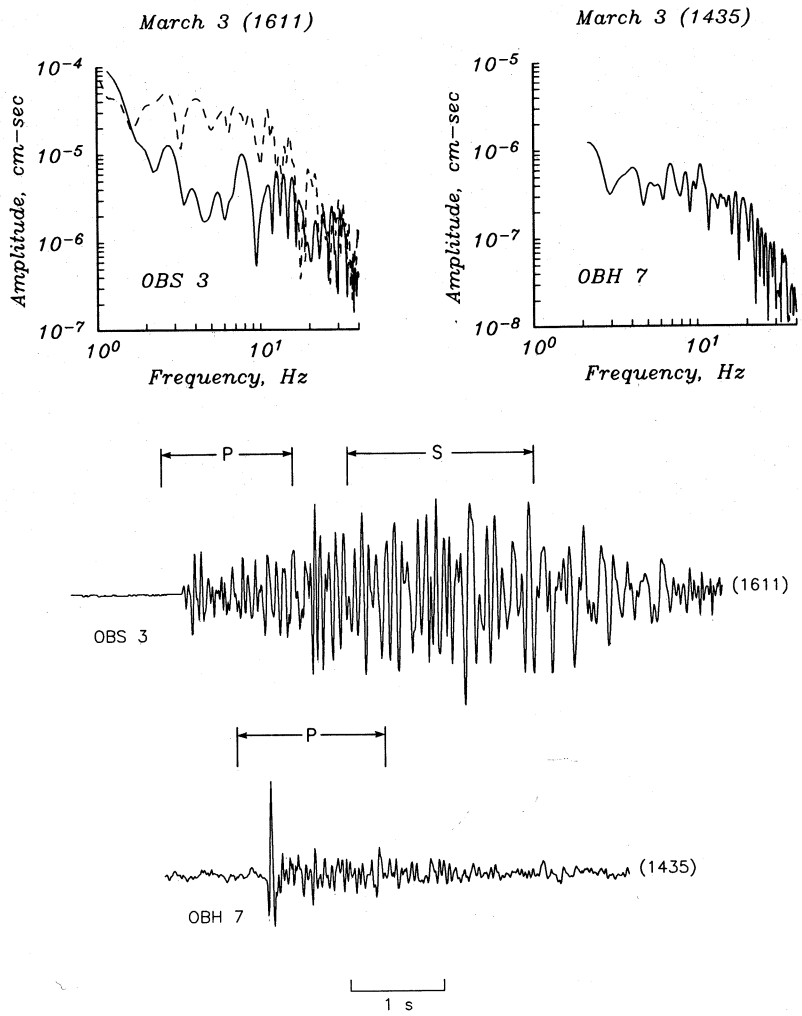

Fig. 6. Examples of P (solid curve) and S (dashed curve) displacement spectral amplitude from an OBS 3 vertical channel record and equivalent P displacement spectral amplitude from an OBH 7 record. The time windows used for the calculation of spectra are bracketed by vertical lines; the S wave window begins immediately prior to the S arrival, as indicated on horizontal component seismograms. Data were premultiplied by a pi-prolate window [*Thomson*, 1977]. The Nyquist frequency is 60 Hz for the OBS and 50 Hz for the OBH.

nisms are poorly constrained, and R was taken equal to 1 for both P and S waveforms. For events beneath the inner floor, values of R for P and SV waves were calculated from the composite fault plane solution shown in Figure 5*a*. The values used for ρ_0, V_p, and V_s were 2.9 g/cm^3, 6.5 km/s, and 3.7 km/s, respectively.

The correction factor K depends on the type of receiver (OBS or OBH), the material properties of the ocean and the uppermost crust, the angle of incidence of the upcoming wave, and the wave type (P or SV). We calculated values of K from plane wave theory; the P and S velocity and density of the uppermost crust were taken to be 3.5 km/s, 2.0 km/s, and 2.9 g/cm^3, respectively, and the P velocity and density of water were taken to be 1.5 km/s and 1.0 g/cm^3, respectively. For the earthquakes under consideration the incidence angles at the seafloor of P and SV waves are 20°–30°. For P waves, K is approximately 1.5 and slowly varying at these angles of incidence, and the factor to reduce equivalent displacement data from an OBH to the vertical component is near unity. For SV waves, K varies from 0.6 to 0.8 at these incidence angles and was taken to be 0.7.

Seismic moments obtained for five events from OBS 3 waveforms and for 39 events from OBH 7 records are listed in Table 2. Corner frequencies estimated from S wave spectra are also given. Seismic moments calculated from P waveforms recorded on the OBS agree well with those obtained from S waveforms. Moments obtained from OBS and OBH records agree to within about a factor of 2. The largest recorded event, located beneath the rift mountains, had a seismic moment of about 10^{20} dyn cm (10^{13} N m). The smallest recorded earthquakes, located generally within the network and beneath the inner floor, had seismic moments of about 10^{17} dyn cm.

The distribution of earthquakes by seismic moment is often cast in the form

$$\log N(M_0) = A - BM_0 \qquad (2)$$

where $N(M_0)$ is the number of events with moment greater than M_0 for a given region and time interval. The data from OBH 7 records given in Table 2 are displayed in this form in Figure 7. A group of 19 events located within about 1 km of the trend of inner floor seismic activity (Figure 2) is treated separately from 20 other events with epicenters east of the first group. For the eastern group of 20 earthquakes, located primarily beneath the rift mountains, linear regression yields a B

TABLE 2. Moments and Corner Frequencies for Selected Earthquakes

Event		OBH 7	OBS 3		
Date	Time, UT	$M_0(P)$, dyn cm	$M_0(P)$, dyn cm	$M_0(S)$, dyn cm	f_c, Hz
Feb. 22	2322	4×10^{19}			
Feb. 22	2324	7×10^{18}			
Feb. 23	1127	6×10^{18}			
Feb. 24	107	1×10^{18}			
Feb. 24	734	2×10^{17}			
Feb. 24	757	4×10^{17}			
Feb. 24	907	1×10^{19}			
Feb. 24	1055	4×10^{18}			
Feb. 24	2151	4×10^{19}	2×10^{19}	3×10^{19}	7
Feb. 24	2223	2×10^{18}			
Feb. 25	205	8×10^{18}			
Feb. 25	206	1×10^{19}			
Feb. 25	323	2×10^{18}			
Feb. 25	533	8×10^{18}			
Feb. 25	621	3×10^{17}			
Feb. 25	806	3×10^{18}			
Feb. 25	808	4×10^{18}			
Feb. 25	812	8×10^{18}			
Feb. 25	824	2×10^{18}			
Feb. 25	2106	9×10^{17}			
Feb. 26	14	2×10^{18}			
Feb. 26	349	3×10^{19}	1×10^{19}	1×10^{19}	9
Feb. 26	1729	4×10^{18}			
Feb. 26	1825	2×10^{18}			
Feb. 26	2224	8×10^{18}			
Feb. 28	849	3×10^{18}			
Feb. 28	851	2×10^{19}			
Feb. 28	2333	5×10^{18}			
March 1	1103	6×10^{17}			
March 2	825	4×10^{18}			
March 2	1023	5×10^{18}			
March 3	635	4×10^{19}	2×10^{19}	1×10^{19}	9
March 3	1435	7×10^{18}			
March 3	1611	5×10^{19}	1×10^{20}	1×10^{20}	9
March 3	1715	1×10^{19}			
March 3	2127	8×10^{17}			
March 4	447	4×10^{19}	6×10^{19}	4×10^{19}	9
March 4	636	3×10^{17}			
March 4	1015	3×10^{18}			

value of 0.5 ± 0.1. For inner floor microearthquakes a plot of M_0 versus slant range from OBH 7 suggests that the recorded events with $M_0 < 10^{18}$ dyn cm sample a smaller volume than do events with $M_0 > 10^{18}$ dyn cm. Including only the group of larger events yields $B = 0.8 \pm 0.2$ (Figure 7).

The S wave corner frequencies f_c in Table 2 can be related to the radius r of the equivalent circular source by the relation [e.g., *Brune*, 1970; *Madariaga*, 1976; *Brune et al.*, 1979]

$$r = CV_s/f_c \qquad (3)$$

where V_s is the S wave velocity at the source and C is a factor that depends on the azimuth to the source and a model of the rupture process. Values of C generally range from 0.2 to 0.4, giving values of source radius of about 100–200 m for the five rift mountain events recorded on OBS 3. The implied values for average fault slip and average stress drop for these earthquakes [*Brune*, 1970] are in the range 0.3–10 mm and 1–70 bars (0.1–7 MPa), respectively.

Tomographic Analysis of Travel Time Data

The distribution of seismic sources and receivers in this experiment is sufficient to conduct a tomographic inversion of travel time data to determine the two-dimensional structure of the P wave velocity across the inner floor of the median valley. One indication in paper 1 that lateral heterogeneity in crustal velocity structure might be present in the region of the microearthquake experiment was the distribution of P wave station delay times. These delays, introduced in paper 1 to account approximately for the effects of differing elevation and shallow velocity structure beneath the network stations, were obtained from the mean travel time residuals observed at each station for a group of 10 well-recorded microearthquakes. While the delays at most stations displayed the expected negative correlation with elevation, the delays at OBH 3 and OBH 5, both on the western side of the median valley, were significantly more negative than expected from local water depth (Figure 8). In this section we begin with a brief outline of the tomographic method and the data set, and we follow with a discussion of the sensitivity of the resulting models to the assumptions. We conclude that the available P wave travel time residuals indicate a region of relatively lower velocities at 1–5 km depth confined to the central portion of the median valley inner floor.

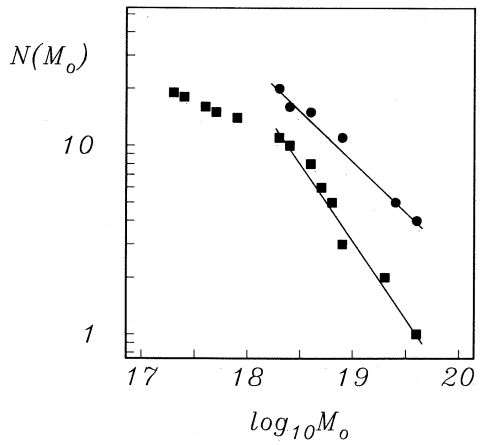

Fig. 7. The number $N(M_0)$ of earthquakes with moment in excess of M_0 for microearthquakes beneath the inner floor (solid squares) and rift mountains (solid circles). The straight lines are least squares fits to the indicated data.

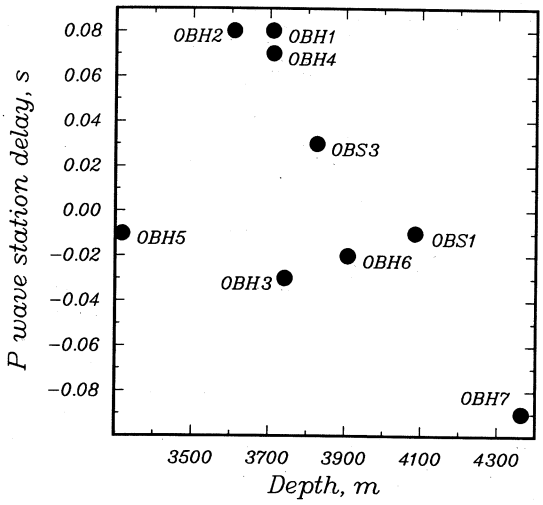

Fig. 8. P wave station delay versus instrument depth for the OBH-OBS network (Figure 2). See paper 1 for a discussion of station delay determination.

Description of the Method

The tomographic method used to invert *P* wave travel times is a variation of the technique developed by *Thurber* [1981, 1983] for simultaneous inversion for earthquake location and velocity structure. Thurber's method incorporates two features that make its use advantageous. First, travel times of first arriving body waves are estimated by a computationally efficient, three-dimensional, approximate ray tracing routine [*Thurber*, 1983]. Second, the model parameterization is flexible and permits an arbitrarily and continuously varying velocity field. The velocity field is represented as a continuous function which depends on the linear average of velocity values at nearby nodes; the locations of nodal points that parameterize the velocity field may be irregularly spaced. Given that the nodes adequately sample the volume to be imaged, velocity models of arbitrary geometry can be readily constructed. Velocity model perturbations are estimated iteratively by solving a linearized set of equations by the Levenburg-Marquardt method of damped least squares. An *F* test on the ratio of mean-square travel time residuals from two successive iterations is the basis for terminating the iterative solution; individual squared residuals are weighted in the manner described in paper 1. Iteration ceases when the ratio of successive travel time residual variances falls below a critical value defined by the 5% level of significance.

The variation of Thurber's method employed here optimizes the velocity structure while holding all four hypocentral parameters to values specified by the starting model. The fixed hypocentral parameter restriction was imposed because of the limited size of the travel time data set. For reasons given below, only six stations were included in the tomographic network, so at most six *P* wave arrival times were included for each earthquake. Since parameter separation would remove four of the possible six arrival time observations for hypocenter relocation [*Pavlis and Booker*, 1980], leaving at most only two observations per earthquake to constrain crustal structure variations, we opted to fix all hypocentral parameters. This approach is based on the assumption that travel time anomalies caused by small perturbations in the hypocentral parameters are independent of those due to small perturbations in the velocity model [*Pavlis and Booker*, 1980]. The fixed hypocentral parameter restriction could, of course, introduce erroneous results if the assumed hypocentral parameters are not "close" to their true values. In a later section we quantify the effects of velocity heterogeneity on the hypocenter location method, we define what is meant by close, and we conclude that fixing hypocentral parameters to values determined by our location procedure is a reasonable approximation.

Even with all hypocentral parameters fixed, the size of the travel time residual data set is insufficient to conduct an inversion for three-dimensional structure. We therefore chose to conduct a two-dimensional inversion for the variation in *P* wave velocity within a cross section perpendicular to the median valley axis.

Summary of Data

The data set to be inverted consists of travel time residuals from 37 earthquakes and nine shots to six stations (Figure 9). The six instruments are located at the southern end of the network and recorded clear *P* arrivals for most earthquakes. The two northernmost ocean bottom hydrophones (OBH 1 and OBH 2) and the northernmost ocean bottom seismometer (OBS 3) were not included in the tomography analysis because few *P* arrivals were well recorded at these stations. The 37 microearthquakes exclude all events with poorly constrained epicenters, events with less than four clear *P* arrivals at the six stations, and the February 22, 2322 UT, inner floor earthquake with a focal depth that is strongly dependent on the assumed source structure (paper 1). Focal depths of 21 of these 37 earthquakes were independently resolved. Of the remaining hypocenters determined for fixed depths, three were located beneath the inner floor and 13 beneath the rift mountains. The microearthquake travel time residuals as utilized in the tomography analysis are not corrected for station delays. Station elevations must therefore be explicitly included in the definition of station locations.

Nine of the 14 shots used for network station location (paper 1) were included as sources in the tomography analysis (Figure 9). For each shot, travel times and source coordinates were adjusted to the seafloor by applying simple water path corrections [*Purdy*, 1982]. Ray entry points at the seafloor for each shot-receiver pair were determined from the range, an estimate of phase velocity derived from the refraction data of *Purdy and Detrick* [1986], and the assumption that the *P* wave propagated in the sagittal plane. The water depth at the ray entry point was taken from the Sea Beam bathymetric map of *Detrick et al.* [1984]. Travel times of shots were corrected for the water segment of the path assuming a uniform velocity of 1.5137 km/s (paper 1). Origin times and locations of shots, so adjusted, remained fixed throughout the tomographic inversion. The five shots not included in the inversion were located above the rough topography of the eastern rift mountains; the simple water path corrections for some source-receiver paths for these shots were subject to errors of as much as 0.1 s because of incorrect water depth. Trial inversions that included data from these shots yielded rms travel time residuals for these five shots approximately 0.03 s larger than for the other nine.

The inclusion in the tomography analysis of travel time data from the shots, whose positions are known to within 20–30 m at one standard deviation (paper 1), helps to constrain the inversion results in two different and important ways. First, the shot data improve the sampling of layer 2 and uppermost layer 3. Second, the shot data are not biased by the velocity structure assumed in the estimation of hypocentral parameters. In the next section we demonstrate that inversions including shot data can be used to discriminate among source structures assumed for hypocentral locations.

Compared with the travel times for an initial source model given by the inner floor structure of *Purdy and Detrick* [1986], the rms travel time residual prior to inversion is 0.13 s. The travel times of *P* waves from the 37 earthquakes to the six stations have a rms residual of 0.11 s; the travel times for *P* waves from the nine shots to the same six stations have a rms residual of 0.18 s. These values exceed the likely uncertainty, about 0.04 s (paper 1), due to errors in reading arrival times, locating sources and receivers, correcting for clock drift, and correcting wave paths from shots to the seafloor. We attribute a significant portion of the excess residual to heterogeneous velocity structure.

Description of Starting Models: Tests of Robustness

The two-dimensional *P* wave velocity model to be estimated by tomographic inversion is defined parametrically by the values of velocity at each of 12 nodes. The nodes are arranged in three vertical columns spaced 6 km apart; the columns are

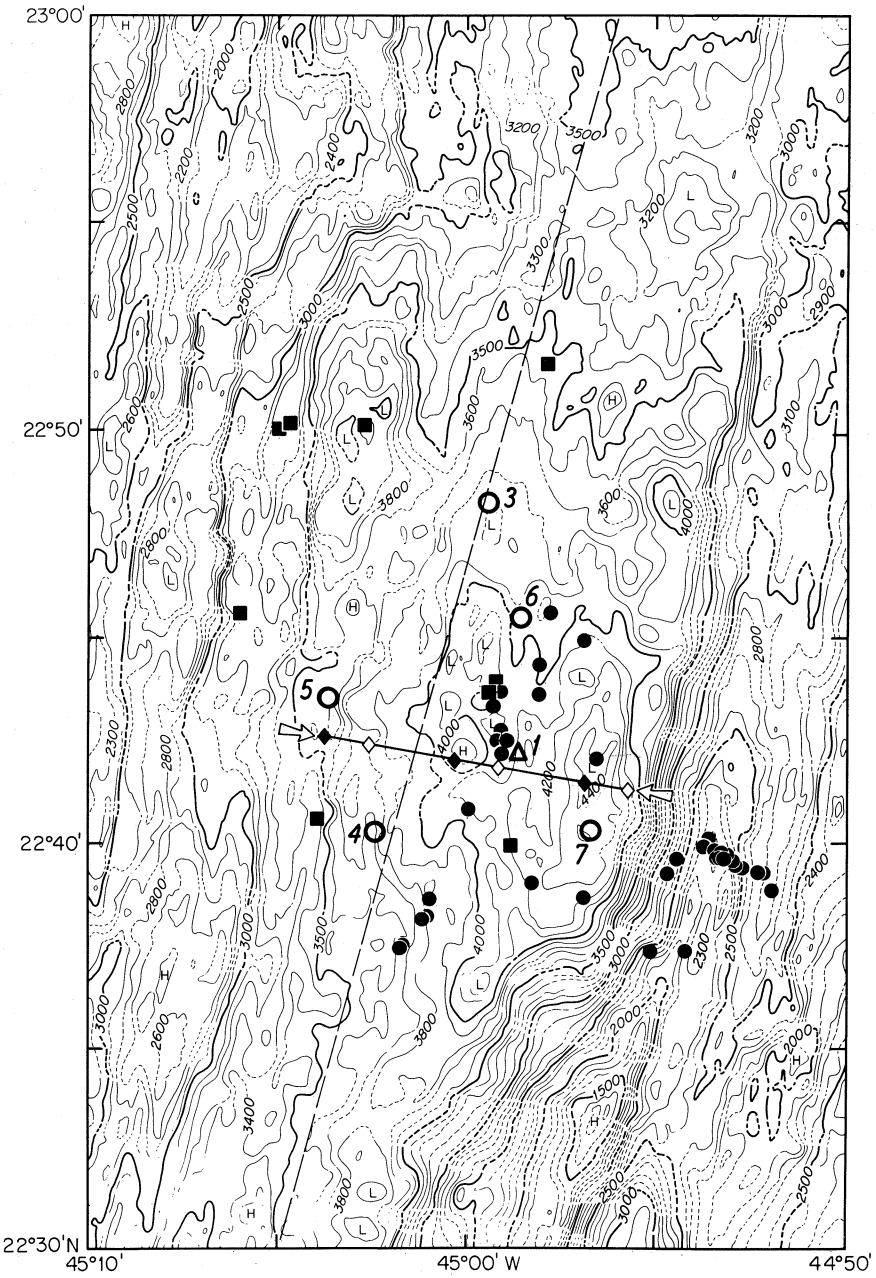

Fig. 9. Positions of microearthquakes (solid circles), ranging shots (solid squares), and ocean bottom instruments (open circles, OBH; open triangle, OBS) included in the tomography analysis. The Sea Beam bathymetry is from *Detrick et al.* [1984]. The dashed line indicates the location of the refraction line of *Purdy and Detrick* [1986]. The solid line marked by arrows is the surface projection of the vertical plane containing parametric velocity nodes (diamonds); solid and open symbols denote two distinct parameterizations (see text).

aligned in a plane oriented perpendicular (N100°E) to the regional trend of the median valley. Each column contains a node at 0, 1, 3, and 5 km depth. The closely spaced shallow nodes were found to be necessary in order to model the steep velocity gradient in the uppermost crust. Several different placements of the nodes with respect to sources and receivers have been considered (Figure 9). Velocity is estimated between nodes by linear interpolation [*Thurber*, 1983]. For all inversions the initial velocity model is laterally homogeneous.

Nonlinear inverse problems require an assessment of the dependence of the final solution upon the assumed initial values of model parameters. We conducted several tests of the influence on the final solutions of the initial velocity model and the assumed source population and hypocentral parameters (Table 3). Two velocity models were considered for both the initial velocity model and the source structure for microearthquake location. These were the median valley structure of *Purdy and Detrick* [1986] obtained from refraction data collected near the site of the microearthquake survey (Figures 1 and 9) and the velocity model obtained by *Detrick and Purdy* [1980] from a refraction experiment on 7-m.y.-old oceanic crust. Hypocentral parameters of the 21 microearthquakes with independently resolved focal depths were calculated for both velocity models. Model-dependent station delays were included in the location procedure. Values of focal depth and origin time calculated with the 7-m.y.-old crustal

structure were systematically shallower and later by about 0.4 km and 0.09 s, respectively, than values estimated for the inner floor crustal structure. These systematic biases produce travel times for the 7-m.y.-old crustal structure that are less, on average, by as much as 0.10 s.

Tomographic inversions of travel times from the 21 microearthquakes with well-resolved focal depths were conducted for each initial velocity structure in order to assess the influence of hypocentral parameters on the tomography results. Inversions 1 and 3 of Table 3 summarize the results for hypocentral parameters based on the 7-m.y.-old and inner floor source structures, respectively. The final rms travel time residual and percent variance reduction are similar for both inversions, indicating that the two inversion solutions model the travel time data equally well. Inspection of the final velocity models, however, indicates that while the relative velocity variations are similar between the two models, the values of velocity at a given node differ by as much as 1 km/s. These results suggest either that travel time data from earthquakes alone do not strongly constrain the absolute values of velocity or that at least one of the sets of hypocentral parameters yields travel time data that are biased by the assumed source structure.

The ambiguous character of these results can be resolved by inclusion of the travel time data from shots. The input to inversions 2 and 4 (Table 3) is identical to that for inversions 1 and 3, respectively, except for the addition of shot data. The relatively small variance reduction and large value of final rms residual for inversion 2 (Table 3) suggest that the travel time data from shots are inconsistent with the earthquake travel time data determined with the 7-m.y.-old source structure. In contrast, the larger variance reduction and smaller final residual for inversion 4 (Table 3) indicate that the travel time data from shots and earthquakes are more nearly consistent when the inner floor structure is assumed for hypocentral locations. For inversions 2 and 4 the values of velocity at well-resolved nodes at 0 and 1 km depth agree to within 0.2 km/s, underscoring the important control of shallow structure by the shot data. At depths of 3–5 km, however, values of velocity differ by as much as 1 km/s between inversions 2 and 4. Also, nodal velocity values differ between inversions 1 and 2 by as much as 1.3 km/s, while velocities obtained from inversions 3 and 4 agree, on average, to within 0.3 km/s at nodal locations well resolved in both inversions. We conclude from these results that inclusion of travel time data from shots is capable of resolving the ambiguity in velocity models obtained from microearthquake travel time data alone. In particular, the microearthquake hypocentral parameters calculated with the 7-m.y.-old source structure are less compatible with the travel time data from shots than are those calculated with the inner floor structure.

It is important to note that these results do not prove that the hypocentral parameters obtained with the one-dimensional inner floor velocity model are unbiased. The possibility remains that our location method is not adequate for locating events in a laterally heterogeneous structure. We address this point in a later section.

We also conducted a tomographic inversion (inversion 5 in Table 3) using travel time data only from the nine shots. The resulting model of velocity heterogeneity is similar to that of inversion 4 for all model parameters except those at 5 km depth. As is expected, the deeper structure is poorly constrained by the shot data because of the comparatively small source-receiver separation for most paths. An examination of well-resolved eigenvectors confirms our earlier inference that the explosive data principally constrain the structure of the upper crust (0–3 km depth). Poorly resolved eigenvectors have large components associated with velocity nodes in the lower crust and, to a lesser extent, within the eastern nodal column. The trace of the resolution matrix, which provides an estimate of the number of resolvable pieces of information intrinsic to a data set [*Wiggins*, 1972], equals 4.6. For comparison, the trace of the resolution matrix for inversion 3, utilizing only data from earthquakes with well-resolved focal depths, is also equal to 4.6. For the latter inversion, well-resolved eigenvectors generally constrain crustal structure only below 3 km depth.

TABLE 3. Summary of Tomographic Inversions

Inversion	Source Structure, m.y.	Inital Structure, m.y.	Data*	r_i, s	r_f, s	s^2, %
1	7	7	B	0.13	0.07	76
2	7	7	A,B	0.15	0.12	37
3	0	0	B	0.11	0.07	67
4	0	0	A,B	0.14	0.09	57
5	···	0	A	0.18	0.12	59
6	0	0	A,C	0.13	0.08	62
7	0	0	A,D	0.14	0.10	54
8	0	7	A,B	0.14	0.09	56

Inversions are numbered for reference; see text. The source structure and initial structure are the laterally homogeneous models used to determine hypocentral location and the initial velocity model for tomographic inversion, respectively; the models are designated by appropriate seafloor age as 7 m.y. [*Detrick and Purdy*, 1980] or 0 m.y. [*Purdy and Detrick*, 1986]. The quantities r_i, r_f, and s^2 are the initial and final rms travel time residual and the variance reduction, respectively.

*The code for the subset of sources of travel time data used in the tomographic inversion and the number of travel time observations for each set of data are as follows: A, 9 shots, 52 observations; B, 21 microearthquakes with independently resolved focal depths, 104 observations; C, 37 microearthquakes with well-resolved epicenters, 171 observations; D, 19 inner floor events, 87 observations.

In addition to the above tests of the inversion procedure we varied the subset of microearthquake sources included in the set of travel time data, and we varied the initial velocity model from that assumed in calculating hypocenters. Inversion 6 is similar to inversion 4 except that travel times from all 37 microearthquakes with well-resolved epicenters are included in the data set. The effect of including more events is principally to increase ray path sampling. Nodal values of velocity in the final solution of inversion 6 agree to within 0.2 km/s of the values for the solution from inversion 4 at all but one node. The trace of the resolution matrix for inversion 6 equals 7.3. It is evident from a comparison of this value with those for inversions 3 and 5 that while the travel time data from shots and earthquakes each separately provide a comparable number of independent constraints, taken together the two data sets constrain complementary portions of model parameter space. Inversion 7 is similar to inversions 4 and 6 except that the microearthquake travel time data set is limited to the 19 inner floor events. Nodal velocity values agree to within 0.2 km/s with those from inversion 4. These tests demonstrate that the final velocity models are robust with respect to the subset of microearthquake travel time data that is utilized in the inversion.

Inversion 8 (Table 3) is identical to inversion 4 except for the initial velocity structure. The final rms travel time residual and variance reduction for inversions 4 and 8 are nearly identical. Values of nodal velocity agree at all but two poorly

	Inversion 3				Inversion 6		
	West	*Central*	*East*		*West*	*Central*	*East*
Velocity, km/s *Percent deviation* *Resolution*	3.6 20±1 0.2	3.0 1±1 0.1	3.0 --- 0	z=0	3.5 17±3 0.6	3.2 5±3 0.3	2.8 -7±1 0
	4.8 8±1 0.3	4.4 -3±2 0.4	4.5 --- 0	z=1	5.0 11±2 0.7	4.0 -11±2 0.7	4.2 -8±2 0.4
	7.0 9±1 0.3	6.0 -6±2 0.5	6.0 -6±2 0.6	z=3	6.5 1±2 0.7	6.3 -2±2 0.7	6.4 0±2 0.6
	7.9 11±2 0.6	7.1 0±2 0.8	7.4 5±1 0.9	z=5	7.9 12±3 0.7	7.2 1±2 0.9	7.6 7±1 1.0

Fig. 10. Nodal values of P wave velocity, associated error, and resolution for inversions 3 and 6 (Table 3). Columns labeled west, central, and east denote the relative locations of nodal columns across the inner floor. The depth z of each node relative to the 3900-m isobath is indicated in kilometers. The error in percent velocity deviation is given at the one standard deviation level of confidence for nodes with nonzero resolution. See text for a discussion of resolution.

resolved seafloor nodes to within 0.2 km/s for the solutions from the two inversions. This degree of agreement suggests that the final velocity model is independent of the assumed initial structure.

Results of Tomographic Inversions

Representative solutions to the tomographic inverse problem are depicted in Figures 10 and 11. Figure 10 gives the values of P wave velocity and associated error and resolution at each of the 12 parametric nodes for inversions 3 and 6 (Table 3). The linearly interpolated two-dimensional velocity structure resulting from inversion 6 is shown in Figure 11. The error is the standard deviation in the percent difference between the final nodal velocity and the initial value. Parameter resolution values, obtained from the diagonal elements of the resolution matrix [*Wiggins*, 1972; *Jackson*, 1972], provide approximate estimates of the ability of the data to resolve the parameter in question. From an inspection of the full resolution matrix we may make the following generalizations. A resolution value in excess of 0.6 (Figure 10) indicates that more than approximately 60% of the estimated velocity value is contributed by structure near the associated nodal location; regions near nodes immediately above or below the node in question contribute about 10–20% each to the estimated velocity value. Because of the large horizontal spacing between nodes (6 km), little horizontal averaging of velocity parameters is generally observed. A resolution value in the range of 0.4–0.6 indicates that 30–50% of the estimated velocity value depends on structure near the corresponding nodal location, while the volumes surrounding nodes above and below contribute approximately 20–30% each to the estimated velocity value. Nonzero resolution values less than 0.4 correspond either to vertical averaging over an entire nodal column or to a significant degree of horizontal averaging of model parameters. Resolution values of zero denote model parameters unconstrained by the data.

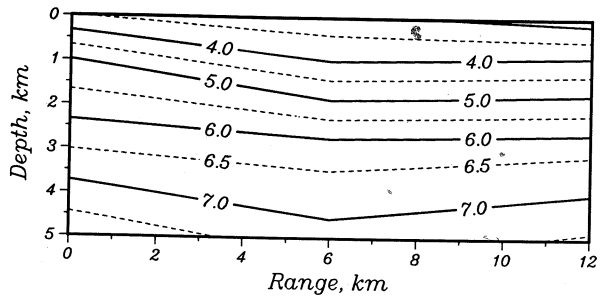

Fig. 11. Two-dimensional model of P wave velocity beneath the median valley inner floor resulting from tomographic inversion of travel times (inversion 6, Table 3). Velocity values are obtained by two-dimensional linear interpolation from the nodal velocity values in Figure 10; the contour interval is 0.5 km/s. The surface trace of the cross section is shown in Figure 9 (nodes at open diamonds).

The two-dimensional velocity models resulting from tomographic inversion indicate that P wave velocities at 1–5 km depth beneath the central median valley inner floor are significantly lower than in surrounding regions (Figures 10 and 11). The velocity contrast is most pronounced between the central and western inner floor. For inversions 4–8 the velocity contrast is largest (0.4–1.0 km/s) at 0–2 km depth, indicating that upper crustal P wave velocities are 10–20% higher beneath the western inner floor than along the center. The average velocity contrast over this depth range is not dependent on the initial velocity model. For these same inversions the velocity below about 2 km depth is 0.2–0.8 km/s, or about 5%, higher beneath the western inner floor than along the center. Velocity contrast between the eastern and central inner floor at shallow depth (0–2 km) is poorly resolved by the available data (Figure 10). Resolution improves at 3–5 km depth, with velocities higher by several percent beneath the eastern inner floor than in the center. An inversion identical to inversion 6 but with each column of nodes shifted westward by 2 km (Figure 9) yielded a velocity solution nearly indistinguishable from that in Figures 10 and 11.

It should be emphasized that because of the coarse horizontal spacing between adjacent nodes in the velocity parameterization, the inversion solutions are laterally smoothed representations of the crustal structure. While the tomographic results demonstrate that P wave velocities are systematically lower within the narrow volume of crust beneath the central inner floor, the detailed form of the velocity structure on a lateral scale less than the nodal separation cannot be specified. Improved resolution of lateral heterogeneity of velocity structure beneath the Mid-Atlantic Ridge median valley must await experiments that provide a denser sampling of the crustal volume to be imaged.

EFFECTS OF VELOCITY HETEROGENEITY ON HYPOCENTER LOCATIONS

The hypocentral parameters of microearthquakes reported in paper 1 and in Table 1 were calculated under the assumption of a laterally homogeneous velocity model [*Purdy and Detrick*, 1986]. Both the rugged topography of the rift mountains and the laterally heterogeneous velocity structure of the median valley inner floor obtained by tomographic inversion call this assumption into question. We have consequently evaluated the effects of velocity heterogeneity on hypocentral locations by means of three-dimensional ray tracing. As we demonstrate below, a comparison of travel time calculations for heterogeneous and homogeneous models indicates that the hypocentral parameters calculated for the homogeneous structure are generally reliable. Two separate models of lateral heterogeneity have been examined. First, a model representing the velocity heterogeneity associated with topographic relief was tested to assess the accuracy of earthquake locations beneath the eastern rift mountains. Second, the two-dimensional model obtained from tomographic analysis was tested to determine the effects of heterogeneity on the locations of microearthquakes beneath the inner floor.

We adopted the following procedure for constructing these velocity models. A three-dimensional grid of P or S wave velocity values was used to define a set of cubic splines from which values of velocity and its first and second spatial partial derivatives were obtained within the model. The method employed the tensor product of splines under tension [*Cline*, 1974], which incorporates a norm that minimizes the curvature of the functional representation, thus effectively limiting the magnitude of unwanted oscillations of the spline fit. The values of velocity and its spatial partial derivatives as calculated from the spline representation were inspected to assure smoothness and accuracy.

Rift Mountain Model

For the model of rift mountain topography we assume that surfaces of constant velocity are simple downward translations of seafloor topography, that is, the velocity is a uniform function of the depth beneath the seafloor. One justification for this simple model is the demonstration by *Purdy and Detrick* [1986] that the crustal structure beneath the inner floor is similar to normal oceanic crust, so that thermal and lithologic contributions to lateral velocity variations associated with crustal aging are likely to be less important than those associated with topographic relief. Since a major contributor to the relief is normal faulting [e.g., *Macdonald and Luyendyk*, 1977], and since the results of this study suggest that active normal faults extend to the base of the crust, simple translation of crustal velocity structure across major faults is a reasonable working hypothesis. For simplicity, we do not include the seismic velocity heterogeneity of the inner floor as documented by the tomographic analysis in this first model.

A two-dimensional P wave velocity model consistent with these assumptions is shown in Figure 12. The model includes a flat inner floor and represents the inner rift mountains by a steep rise of 1.8 km over a horizontal distance of 5 km. A sine function was used to describe the topographic relief across this rise. The P wave velocity as a function of depth beneath the seafloor was taken to be the piecewise exponential structure used by *Purdy and Detrick* [1986] to model the travel times along the inner floor (Figure 12*a*).

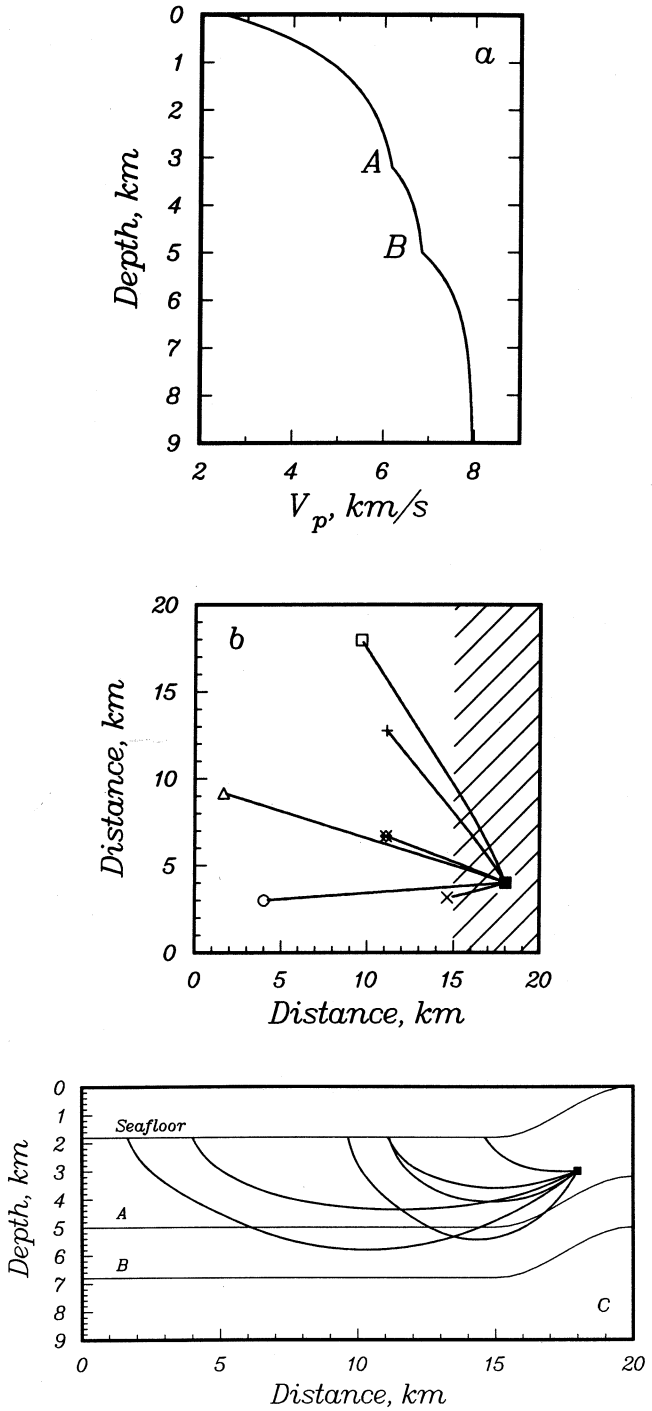

Fig. 12. Two-dimensional velocity model adopted to approximate the effect of rift mountain topography on crustal structure. Velocity contours follow topography. (*a*) P wave velocity versus depth beneath the seafloor, from *Purdy and Detrick* [1986]. (*b*) Representative ray paths in plan view for a source beneath the rift mountains (solid square). The cross-ruled region represents the rift mountains. (*c*) Cross section of model and representative ray paths from a rift mountain earthquake (solid square) at a depth of 3 km below the zero datum. Lines marked A and B correspond to the inflection points of the velocity model in Figure 12*a* at the top of layer 3 and the top of the Moho transition zone, respectively.

Seismic rays were traced through the model of Figure 12 using two complementary methods. First, a "shooting" routine [*Lee and Stewart*, 1981] was employed to explore the general effects of topography upon ray paths. The shooting method is

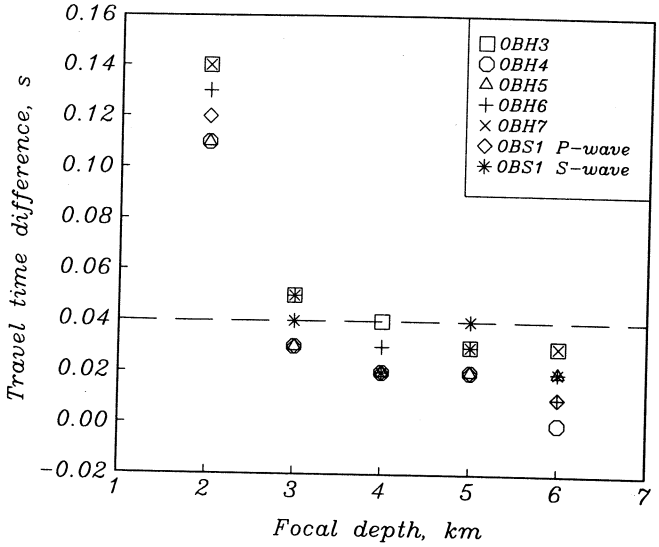

Fig. 13. Differences in travel times for P and S waves from a rift mountain microearthquake between the two-dimensional velocity model of Figure 12 and the laterally homogeneous model of *Purdy and Detrick* [1986]. Travel time differences are for the station and epicenter positions shown in Figure 12*b* for various depths of focus below the zero datum in Figure 12*c*. The "picking error" of 0.04 s (paper 1) is indicated by the dashed line.

an efficient initial value formulation which does not incorporate control over the final end point of the ray. We examined hundreds of P wave ray paths for different source positions beneath the rift mountain portion of the model. Results of these calculations allow us to conclude that ray paths of P waves from sources with shallow depths (within 1–2 km of the seafloor) deviate from a vertical plane because of upper crustal lateral heterogeneity. In contrast, paths from sources deeper than about 2 km beneath the seafloor to positions within the inner floor lie within or very close to a vertical plane. P wave ray paths from these deeper sources are not noticeably perturbed by the laterally variable structure associated with topographic relief.

Second, an approximate ray tracing routine [*Thurber*, 1983], which does not attempt to solve the ray equations, was used to estimate the P and S ray paths between a specified source and receiver. These estimates served as initial ray paths to the "bending" routine of *Pereyra et al.* [1980]. The bending method is a boundary value formulation in which the endpoints of a ray and an initial estimate of a stationary ray path are specified. The results of ray-bending calculations are summarized in Figure 13. Figure 13 shows the P and S wave travel time differences between the laterally homogeneous (Figure 12*a*) and laterally heterogeneous (Figures 12*b* and 12*c*) velocity models for six stations; the S velocity structures are determined from the P wave structures of Figure 12 assuming $V_p/V_s = 1.75$. The six fixed receiver positions (Figure 12*b*) approximate those of actual stations which routinely recorded arrivals from rift mountain earthquakes.

Results from the ray-bending calculations indicate that travel times (Figure 13) and ray paths of P and S arrivals from sources deeper than about 2 km below the seafloor are similar for both the laterally homogeneous and heterogeneous velocity models. The average travel time difference for sources deeper than 2 km is about 0.03 s (Figure 13), a figure less than our estimated travel time picking error (paper 1) of 0.04 s.

As a final check, we inverted the synthetic travel times generated from the ray-bending calculations and the laterally heterogeneous P and S velocity models with the same laterally homogeneous velocity structure and hypocentral location procedure used for our microearthquake data; station delays were recalculated for the new synthetic travel time residual data set in accordance with our procedure in paper 1. In agreement with our results above, estimated focal depth and epicentral coordinates of rift mountain earthquakes deeper than 3 km beneath the seafloor are within 0.3 km of their correct values. These results indicate that the formal errors given by the location procedure give reasonable estimates of the uncertainty in hypocentral parameters. In contrast, locations of sources less than 3 km beneath the seafloor were poorly resolved, and the convergence rate of the iterative location procedure was unusually slow. On the basis of these travel time calculations and source relocations we conclude that the hypocenters of the seven well-recorded rift mountain earthquakes reported in paper 1 are accurately estimated despite the large topographic relief and associated lateral heterogeneity in velocity structure.

Inner Floor Model

For the P velocity model of the inner floor the solution to the tomographic inversion was merged with the refraction results [*Purdy and Detrick*, 1986]. Within the central region of the two-dimensional model (Figure 14), P wave velocity versus

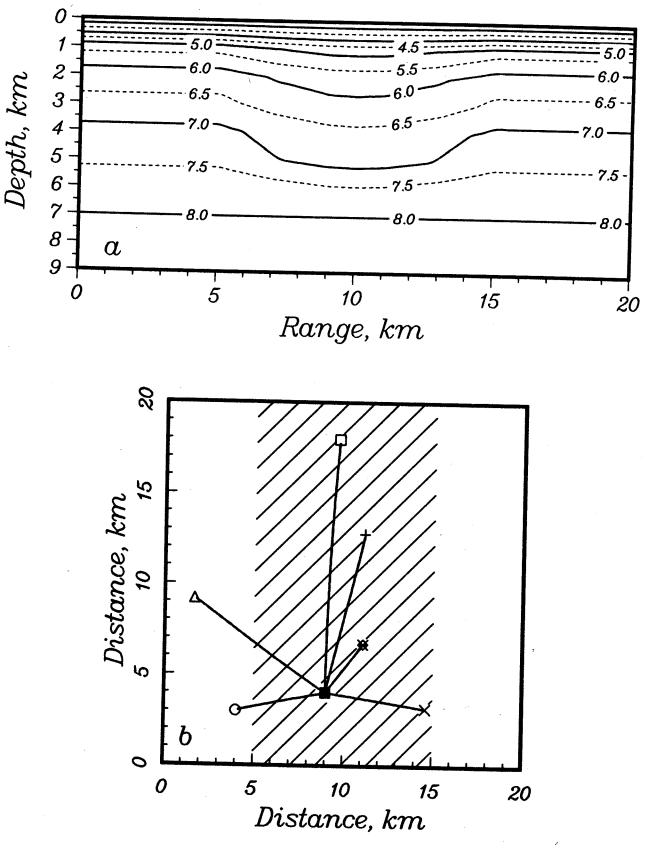

Fig. 14. Two-dimensional velocity model used to evaluate the effects of lateral heterogeneity on hypocentral locations beneath the inner floor. (*a*) Cross section through the model. Contours of P wave velocity are in kilometers per second. (*b*) Plan view of the model. Selected ray paths are shown for a source (solid square) at 6 km depth. Receiver symbols are the same as in Figure 13. The cross-ruled area indicates the region of anomalously low velocities in the middle to lower crust.

depth follows Figure 12*a*. To either side of the central region, velocity increases smoothly with distance by a depth-dependent amount that agrees with the results of tomographic inversion. The functional form of this increase is taken to be a sine function with a full wavelength of 10 km. As discussed earlier, the precise width of the low-velocity region of the central inner floor crust and the detailed shape of the velocity contours are not well resolved by the tomographic analysis. The S wave velocity structure was obtained from the P wave structure assuming $V_p/V_s = 1.75$.

For inner floor microearthquakes, most paths between sources and receivers are nearly straight lines. Because of this simple geometry, the effects of lateral heterogeneity will be confined principally to travel times. Extensive ray-shooting calculations to explore for anomalous travel path effects were therefore not performed with this structure. The ray-bending method was used to compare travel times for the laterally homogeneous and heterogeneous velocity models for a source beneath the inner floor and receiver locations as depicted in Figure 14. The fixed receiver locations in Figure 14 mimic those of the experiment and are identical to those of Figure 12*b*. Travel time differences between the two structures are shown in Figure 15. While travel times to stations within the central inner floor are largely unaffected by the laterally heterogeneous velocity, significant travel time differences are apparent for all source depths at stations outward of the axial low-velocity region (compare stations OBH 5, OBH 4, and, to a lesser degree, OBH 7 in Figures 15 and 14*b*).

The effect of these travel time differences on hypocenter locations was evaluated by using the travel times calculated for the heterogeneous model as input to the location procedure employed for the microearthquake data. In order to be consistent with our location procedure (paper 1), station delays were recalculated for the new travel time data set. The range in station delays (0.10 s) is comparable to the range in travel time residuals (0.12 s) in Figure 15, though the delays and residuals at individual stations differ. Epicentral coordinates and focal depths calculated for the synthetic travel time data were, on average, within 0.3 and 0.5 km, respectively, of their correct values. In comparison with the known locations, calculated focal depths were systematically underestimated. Estimated origin times were within 0.01 s of their correct values.

These calculations indicate that hypocentral parameters presented in Table 1 and paper 1 for inner floor microearthquakes are robust with respect to the effects of known lateral heterogeneities in velocity structure. This conclusion must be tempered by the realization that the laterally heterogeneous structure indicated by the tomography analysis was obtained with fixed earthquake hypocenters. The travel time data from shots, as noted above, provide important information on shallow crustal heterogeneity but little information on lateral variation in structure at greater than 3 km depth. Any portion of the deeper structure that trades off with changes in hypocentral location therefore is not included in the solutions to the tomographic inversion. The possibility remains for some bias in hypocentral positions and earthquake travel times associated with such an unresolved component of structural heterogeneity.

From the above results we can estimate the contribution from source mislocation to travel time anomalies and evaluate our assumption, utilized in the tomography analysis, that observed travel time residuals are due principally to path effects.

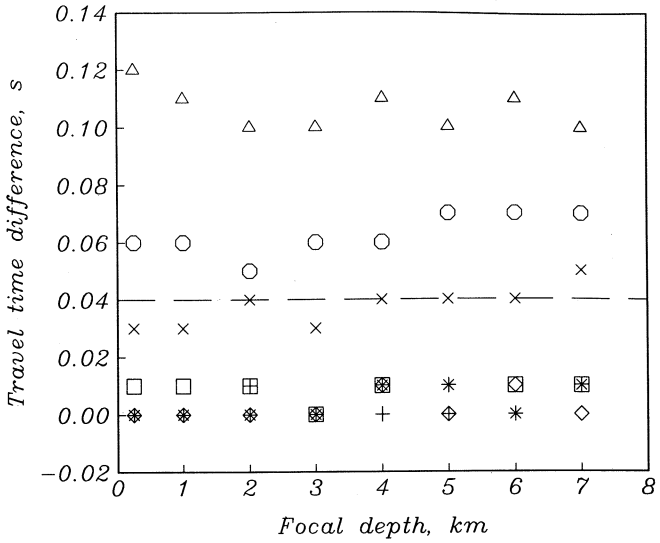

Fig. 15. Differences in travel times for P and S waves from an inner floor microearthquake between the laterally heterogeneous velocity model of Figure 13 and the laterally homogeneous model of *Purdy and Detrick* [1986]. Travel time differences are for the station and epicenter positions shown in Figure 14*b* for various depths of focus below the seafloor. Symbols for stations are as in Figure 13. The "picking error" of 0.04 s (paper 1) is indicated by the dashed line.

For the average error quoted above for hypocentral parameters the travel time anomaly due to mislocation of a source whose focal depth is about 6 km is expected to be less than 0.07 s. This value is significantly less than the rms travel time residual prior to tomographic inversion and comparable to the final rms travel time residual (Table 3). The attribution of a major component of the initial residuals to path effects is therefore reasonable.

TECTONIC SYNTHESIS

In this section we attempt to place the results of the microearthquake observations and tomographic inversion within the context of Sea Beam bathymetry [*Detrick et al.*, 1984], the source mechanisms of large median valley earthquakes [*Huang et al.*, 1986], and the along-axis variation in inner floor crustal structure indicated by seismic refraction measurements [*Purdy and Detrick*, 1986]. We then present a simple kinematic model of the recent tectonic evolution of the median valley inner floor near the site of the microearthquake experiment.

Related Studies

The Sea Beam bathymetric map [*Detrick et al.*, 1984] provides substantially better resolution of the morphology of the median valley near 23°N than was previously available from single, wide-beam echo sounding data. As may be discerned from Figure 2, south of the along-axis high in the median valley near 22°55′N, there is an elongate axial depression that exceeds 4400 m in depth and abuts the steep scarp of the eastern rift mountains near 22°40′N. The overall length and trend of the depression, on the basis of the 4200-m-depth contour, are about 12 km and N10°E, respectively. The topography of both the inner floor and the rift mountains is asymmetric across the median valley. The rift mountain inner wall is much steeper on the eastern side than on the west. As may be seen in the bathymetric profile displayed in Figure 16, the inner floor in the region of the microearthquake network dips

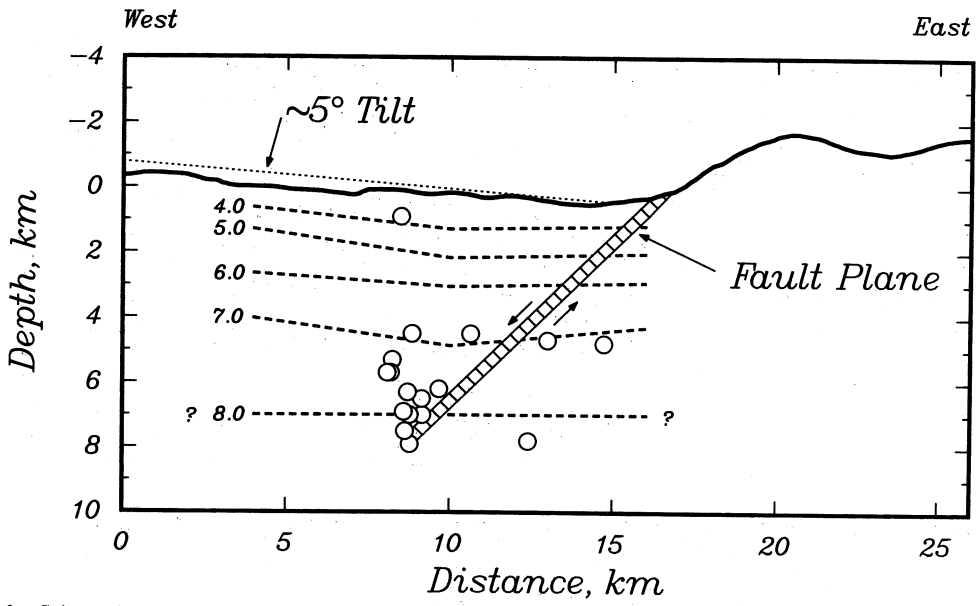

Fig. 16. Schematic cross section of the Mid-Atlantic Ridge median valley at about 22°40′N. Bathymetry and locations of inner floor microearthquakes (circles) are from Figure 3. Contours of P wave velocity (dashed), in kilometers per second, are from Figure 11. The location of the fault plane for recent large ($m_b > 5$) earthquakes is conjectural, but the dip angle and downdip extent are constrained by body waveform inversion [*Huang et al.*, 1986].

eastward at about 5°. At its deepest point the axial depression is 300–400 m deeper than other portions of the inner floor at this latitude (Figure 2).

During the period 1962–1986 the median valley near the 22°40′N axial depression has been the site of several large ($m_b > 5$) earthquakes. Focal mechanisms of three of the largest of these earthquakes determined by an inversion of long-period teleseismic P and S waveforms [*Huang et al.*, 1986] are similar to the normal faulting mechanisms of inner floor microearthquakes at this site (Figure 5) (paper 1). Epicentral locations of these earthquakes are constrained by the local bathymetry and estimates of the water depth above the epicenter from water column reverberations in the P wave trains [*Huang et al.*, 1986]. For example, a water depth of 4000 m above the epicenter of the initial event ($m_b = 5.3$) of an earthquake swarm on June 28, 1977 [*Huang et al.*, 1986], constrains the epicentral location to be near or within the 22°40′N axial depression. The maximum depth of slip beneath the seafloor and the along-axis extent of rupture for the three large earthquakes are constrained by the centroid depth and the duration of the source time function to be approximately 3–5 and 10–15 km, respectively [*Huang et al.*, 1986]. In general, the strike and area of the seafloor projection of the fault surfaces for these large earthquakes are similar to the azimuthal trend and areal extent of the 22°40′N axial depression. These results are consistent with the simple hypothesis that a single large fault plane, with a downdip length of 5–7 km and an along-strike extent of 10–15 km, undercuts the 22°40′N axial deep and has been the site of the several large earthquakes observed teleseismically in this region during the last 25 years. This hypothesis is depicted schematically in Figure 16; though the earthquake mechanisms are consistent with either a westward or eastward dipping fault plane, because of the asymmetric seafloor topography we prefer a westward dipping fault plane that cuts the seafloor at the base of the eastern rift mountains. With this geometry the inner floor microearthquakes cluster about the lower portions of this fault plane (Figure 16).

The P wave velocity structure of the inner floor crust near the axial depression is well constrained along strike by the seismic refraction line of *Purdy and Detrick* [1986] and across strike by the tomography analysis presented above. *Purdy and Detrick* [1986] have demonstrated that the crustal thickness and P wave velocity structure beneath the central inner floor, except for the lower velocities in layer 3, are similar to those of nearby 7-m.y.-old crust [*Detrick and Purdy*, 1980]. In particular, the layer 2/layer 3 and crust-mantle transition zones are well developed, and the uppermost mantle has a nearly normal P wave velocity (7.9 km/s) and a positive gradient of velocity with depth. This crustal structure, in addition to the depth distribution of microearthquakes, constitutes strong evidence against recent magmatic activity beneath the inner floor of this segment of the median valley (paper 1 and *Purdy and Detrick* [1986]).

A Tectonic Model of Crustal Extension

A simple kinematic model of block faulting can satisfy these observations of bathymetry, earthquake source parameters, and seismic structure. In the model the westward dipping fault of Figure 16 separates the eastern rift mountain and inner floor tectonic provinces. This boundary fault extends downdip at an angle of about 45° from the seafloor at the foot of the crestal mountains to a depth of 5–8 km beneath the inner floor and extends along axis for a distance of at least 10 km. Repeated seismic slip on the boundary fault accommodates inner floor extension and rift mountain uplift and gives rise to progressive rotation of the inner floor fault block. The combination of an eastward dipping inner floor with the exposed footwall scarp forms an asymmetric axial depression on the seafloor above the boundary fault (Figure 16).

The westward dipping boundary fault is associated in this kinematic model with the rupture plane of at least some of the large earthquakes that have occurred in this region in the last 25 years. The dimensions and orientation of the boundary fault are consistent with the rupture dimensions and epicentral characteristics indicated by waveform inversion [*Huang et al.*,

1986]. By inference the microearthquakes observed beneath the inner floor are also associated with the westward dipping boundary fault, either on the main fault itself or on nearby secondary faults. That the focal depths of the microearthquakes (5–8 km) are similar to or slightly greater than the maximum depth of slip for the large earthquakes (approximately 5 km) [*Huang et al.*, 1986] lends support to this inference. Further support is provided by the similarity between the focal mechanisms of the smallest ($M_0 = 10^{17}$–10^{19} dyn cm, Table 2) and largest ($M_0 = 10^{24}$–10^{25} dyn cm [*Huang et al.*, 1986]) earthquakes observed (paper 1) and the agreement between the along-axis extent and strike of the fault planes of the large earthquakes [*Huang et al.*, 1986] and the observed distribution of inner floor microearthquakes (Figure 2).

The kinematic block faulting model permits order of magnitude estimates to be made of the time required to form the axial depression as well as the number and frequency of large earthquakes necessary to create the 300–400 m of associated relief. We assume, for simplicity, that the full spreading rate is currently being accommodated across the westward dipping boundary fault, that is, that neither magmatic injection nor faulting on the western boundary of the median valley contribute significantly at present to plate spreading. By this assumption the vertical component of relative motion between the inner floor and the eastern rift mountains is equal to the full spreading rate of 27 mm/yr [*Minster and Jordan*, 1978]. If this geometry of faulting persisted unmodified for a finite duration, then the minimum time required to form the axial depression is approximately 10^4 years. By this line of reasoning, we can also estimate the number of large earthquakes which would have occurred along the boundary fault of the axial depression within the past 10^4 years. Assuming that the events studied by *Huang et al.* [1986] are representative of large earthquakes along the Mid-Atlantic Ridge median valley, we may infer that the average fault slip during large earthquakes is about 0.5 m. Thus if the axial depression is principally the result of seismogenic slip associated with large earthquakes, about 10^3 large events are necessary to yield 300–400 m of relief. This number is equivalent to a recurrence period of about 10 years. This compares with four earthquakes with $m_b \geq 5.5$ in the general vicinity of the axial depression near 22°40′N in the last 25 years. These simple calculations, while not conclusive, support the view that both the ongoing extension of the young oceanic lithosphere and the generation of the axial depression near 22°40′N are the result of repeated normal-faulting earthquakes during the past 10^4 years.

DISCUSSION

The seismicity, earthquake source properties, and seismic velocity structure observed during this experiment characterize this segment of the Mid-Atlantic Ridge as one that is currently undergoing active tectonic extension in the absence of crustal magmatic activity. The simple kinematic model of crustal extension and block faulting presented above suggests that this state has persisted for at least the last 10^4 years. Several aspects of these results are deserving of further discussion. These include possible explanations for the low values of *P* wave velocity beneath the central inner floor, the fate of the boundary fault at depth, and the implications of our findings for the along-axis variability of spreading center processes, particularly along the portion of the Mid-Atlantic Ridge south of the Kane Fracture Zone.

The tomographic inversion of travel time data and the refraction analysis of *Purdy and Detrick* [1986] indicate relatively low *P* wave velocities at 1–5 km depth within a narrow volume (less than 10 km wide) beneath the central inner floor. Lateral variation in crustal temperature structure can contribute to some, but not all, of the observed velocity heterogeneity. The temperature derivative of *P* wave velocity in oceanic gabbro is about -6×10^{-4} km/s/K [*Christensen*, 1979]; a lateral temperature contrast of 400 K at 3–5 km depth would account for a horizontal variation in velocity of about 0.25 km/s, or only about one third of the variation indicated in the tomographic inversion solutions (Figure 10). Such a temperature contrast is about the maximum that could be sustained without placing the lower crust beneath the central inner floor outside of the brittle field of behavior for gabbroic material [*Caristan*, 1982].

Purdy and Detrick [1986] attributed the low velocities to the presence of unfilled cracks and voids remaining after rapid cooling of the most recently injected crustal magma body. Such porosity would have to persist despite lithostatic pressures of 1–2 kbar; the observation of significant porosity and fluid permeability at 3 kbar pressure at the Kola deep drill hole [*Kozlovsky*, 1982] suggests that such a situation is at least possible. Purdy and Detrick further suggested that the evolution to the higher and more normal *P* wave velocities that they observed beneath 7-m.y.-old crust occurs as a result of sealing of the cracks and pores by deposition of hydrothermal minerals. By this reasoning, the narrow volume of low velocities beneath the central inner floor (Figure 11) marks the locus of most recent magmatic emplacement, and the evolution of oceanic crustal structure is inferred to be essentially complete within a few hundred thousand years after crustal emplacement. This interpretation attributes the lateral differences in velocity in Figure 11 to a variation with crustal age.

An alternative interpretation of the low *P* wave velocities beneath the central inner floor attributes significance to the coincidence of the zone of reduced velocities and the lower reaches of the inferred boundary fault (Figure 16). It is plausible that a major active fault extending to 5–8 km depth provides a ready route for seawater to penetrate the lower crust. Such penetration may have led to significant hydrothermal alteration and consequent reduction of the *P* wave velocity [e.g., *Christensen*, 1966] in the overlying crustal column. By this scenario, the horizontal velocity variations in Figure 11 are not functions of crustal age. To the contrary, the block of lower velocities presently beneath the median valley inner floor will, by implication, be transported laterally by seafloor spreading processes without a significant increase in *P* wave velocity and will remain a region of anomalously low velocity even at greater crustal ages.

Under these two interpretations of the velocity structure in Figure 11, somewhat different variations of *P* wave and *S* wave velocity across the median valley would be predicted, but the tomographic inversion does not have the spatial resolution necessary to resolve the differences in *P* wave structure, and insufficient *S* wave arrivals were recorded during this experiment to address the *S* wave velocity structure. The along-axis variation in structure is another potential discriminant between the two interpretations. *Purdy and Detrick* [1986] inferred that the crustal structure along this portion of the median valley inner floor is similar for an along-strike distance of 50–60 km, except for a 10- to 15-km-length zone of significantly lower velocity beneath the along-axis high at 22°55′N

(Figure 1). Since such a distance considerably exceeds the length of the axial depression within which the microearthquake experiment was conducted (Figure 2), their observation favors the view that the variation in P wave structure seen in Figure 11 is primarily a function of seafloor age.

The rotation of the inner floor crustal block in the kinematic model of Figure 16 raises the question of the nature of faulting at or below the depth of the deepest earthquakes. Finite rotation requires either that the bounding fault display a listric geometry or that the fault truncate at depth at a ductile shear zone [*Jackson and McKenzie*, 1983; *Brun and Choukroune*, 1983]. Such a zone of ductile shear has been suggested to occur at midcrustal to lower crustal levels on the basis of field observations in ophiolites [*Casey et al.*, 1981]. The focal depths and mechanisms of large earthquakes [*Huang et al.*, 1986] and microearthquakes (Figure 5) at this site constrain the principal fault or faults to be planar or nearly planar to at least 5 km depth (Figure 16); modest lessening of the fault dip angle with greater depth is neither required nor precluded by the locations of microearthquake hypocenters and their associated errors (Figure 3). The nature of the deformation accommodating extension below about 8 km depth is not constrained by available data.

The 100 km of Mid-Atlantic Ridge median valley south of the Kane Fracture Zone can be divided into several distinct spreading center segments or cells [*Schouten and Klitgord*, 1982; *Schouten et al.*, 1985] variously dominated by recent tectonic extension or volcanic and hydrothermal activity [*Karson et al.*, 1987]. The microearthquake network (Figure 2) was located south of a prominent along-axis topographic high near 23°55′N (Figure 1). In the spreading cell hypothesis, along-axis highs correspond to sites of enhanced rates of crustal magma injection and generally higher crustal temperatures [*Whitehead et al.*, 1984; *Crane*, 1985; *Schouten et al.*, 1985]. *Purdy and Detrick* [1986] found that the P wave velocities in the lower crust beneath the axial high near 22°55′N are even lower than elsewhere beneath the median valley inner floor, consistent with this high being a center of comparatively recent magmatic injection. During the period of the microearthquake experiment of this paper, only one earthquake was located in the vicinity of the along-axis high (Figure 2); had additional earthquakes of comparable size occurred during the deployment, the network configuration was such that they would have been readily detected and located. While a period of a few weeks is too short to characterize rates of seismic activity, the low seismicity that we observed for the along-axis high is at least consistent with that region being in a state of higher crustal temperatures and less well developed fault systems than in the region of the axial depression to the south.

In the spreading cell hypothesis, boundaries between adjacent cells are generally along-axis bathymetric lows [*Schouten et al.*, 1985; *Crane*, 1985]. These along-axis lows are often held to correspond principally to intersections with transform faults, small offsets of the ridge axis, or changes in the strike of the axial neovolcanic zone [*Macdonald et al.*, 1984; *Langmuir et al.*, 1986]. The axial depression at 22°45′N, however, appears to be simply a zone of prolonged crustal cooling and extension, rather than an obvious discontinuity in the position or trend of the accretion axis. This result suggests that boundaries to spreading cells along slow spreading ridges can be manifested by regions in which prolonged periods of extension without magmatic injection occur without disruption of the trend of the median valley inner floor. Whether this portion of the ridge axis serves as a boundary between spreading cells over time scales longer than 10^4 years remains to be demonstrated. Further microearthquake studies along axial lows and highs will be required to explore further the relationship between zones of active extension and possible configurations of spreading cells.

CONCLUSIONS

In this paper we report on the microearthquake source parameters and laterally heterogeneous seismic velocity structure of the Mid-Atlantic Ridge median valley near 23°N. In a data set expanded over that in an earlier report (paper 1), a total of 53 microearthquakes were located over a 10-day period; all events occurred beneath the median valley inner floor and eastern rift mountains. Twenty of 23 well-located inner floor epicenters define a line of activity 17 km long having a strike of N25°E. Linear trends were not resolved by the distribution of epicenters in the eastern rift mountains, although the earthquakes in that region displayed considerable temporal and spatial clustering. Earthquakes with well-resolved hypocenters, with the exception of a single shallow event beneath the inner floor, had focal depths of 4–8 km beneath the seafloor; the formal uncertainty in hypocentral coordinates for the better located events is ± 1 km at the 95% confidence level. Composite fault plane solutions determined from seven inner floor events along the linear seismicity trend indicate normal faulting on planes dipping at angles near 45°. Normal faulting mechanisms, although poorly constrained, are also indicated for the rift mountain microearthquakes. The seismic moments of the recorded microearthquakes are in the range 10^{17}–10^{20} dyn cm; the moment-frequency distribution can be described by a B value of 0.8 ± 0.2 for the inner floor and 0.5 ± 0.1 for the rift mountains. Fault dimensions and stress drops for the largest microearthquakes are 200–400 m and 1–70 bars, respectively.

The inner floor seismicity is concentrated near an along-axis depression some 300–400 m deeper than immediately surrounding areas. Sea Beam bathymetry [*Detrick et al.*, 1984] indicates that the floor of the depression tilts eastward at about a 5° angle until it abuts the steeply dipping inner wall of the eastern rift mountains. The region of the along-axis deep has also been the site of several large earthquakes during the last 25 years [*Huang et al.*, 1986]. The along-axis length of the depression, the length of the inner floor seismicity trend, and the fault lengths of the large earthquakes are all about 15 km. These results provide the motivation for a simple kinematic model of the local tectonics of the inner floor. According to the model a major fault bounds the eastern limit of the inner floor within the deep; the fault is about 15 km long, dips westward at about 45°, and extends to 5–8 km in depth. Repeated slip on the fault during major earthquakes, at a rate of about one per 10 years, has led to the formation of the along-axis depression and to the eastward tilt of the seafloor. At the current rate of plate divergence the observed relief could have been achieved in 10^4 years of extension without accompanying magmatic injection.

A two-dimensional tomographic inversion of P wave travel time residuals from microearthquakes and local shots has yielded an image of the lateral heterogeneity in crustal velocity structure across the median valley inner floor. P wave velocities at 1–5 km depth within a narrow zone (less than 10 km wide) beneath the central inner floor are lower by several percent than in surrounding regions. The velocity anomaly is too large to be due to likely lateral variations in crustal tem-

perature. One possible explanation for the low velocities [*Purdy and Detrick*, 1986] is that the region is the site of the most recent local magmatic injection and remains pervasively fractured as a result of rapid hydrothermal quenching of the newly emplaced crustal column. An alternative explanation is that the region is one of anomalously extensive alteration of the middle to lower crust enabled by deep penetration of seawater along the active normal fault bounding the along-axis depression. The along-axis extent of the region of lower velocities indicated by refraction data [*Purdy and Detrick*, 1986] favors the first explanation. By this interpretation the seismic velocity structure at the ridge axis evolves to that of normal oceanic crust within the first few hundred thousand years of crustal emplacement.

Acknowledgments. We thank Leon Gove and Cliff Thurber for providing important elements of the software used in this analysis, John Collins for useful discussions, Bob Detrick for supplying Sea Beam bathymetric data for the area, Laura Kong for help in producing Figure 1, and Laura Doughty for assistance with manuscript preparation. We also thank Don Koelsch, Carleton Grant, and Peter Roberts for technical assistance and the captain and crew of the R/V *Knorr* for their cooperation in carrying out this experiment. Constructive comments by Don Forsyth, a second reviewer, and the Associate Editor improved the manuscript and are appreciated. This research was supported by the National Science Foundation, under grants EAR-8416192 and EAR-8617967, and by the Office of Naval Research, under contract N00014-86-K-0325.

REFERENCES

Brun, J.-P., and P. Choukroune, Normal faulting, block tilting, and decollement in a stretched crust, *Tectonics*, *2*, 345–356, 1983.

Brune, J. N., Tectonic stress and the spectra of seismic shear waves from earthquakes, *J. Geophys. Res.*, *75*, 4997–5009, 1970. (Correction, *J. Geophys. Res.*, *76*, 5002, 1971.)

Brune, J. N., R. J. Archuleta, and S. Hartzell, Far-field *S* wave spectra, corner frequencies and pulse shapes, *J. Geophys. Res.*, *84*, 2262–2272, 1979.

Caristan, Y., The transition from high-temperature creep to fracture in Maryland diabase, *J. Geophys. Res.*, *87*, 6781–6790, 1982.

Casey, J. F., J. F. Dewey, P. J. Fox, J. A. Karson, and E. Rosencrantz, Heterogeneous nature of oceanic crust and upper mantle: A perspective from the Bay of Islands ophiolite complex, in *The Sea*, vol. 7, *The Oceanic Lithosphere*, edited by C. Emiliani, pp. 305–338, John Wiley, New York, 1981.

Christensen, N. I., Elasticity of ultrabasic rocks, *J. Geophys. Res.*, *71*, 5921–5931, 1966.

Christensen, N. I., Compressional wave velocities in rocks at high temperatures and pressures, critical thermal gradients, and crustal low-velocity zones, *J. Geophys. Res.*, *84*, 6849–6857, 1979.

Cline, A. K., Scalar- and planar-valued curve fitting using splines under tension, *Numer. Math.*, *17*, 218–220, 1974.

Crane, K., The spacing of rift axis highs: Dependence upon diapiric processes in the underlying asthenosphere?, *Earth Planet. Sci. Lett.*, *72*, 405–414, 1985.

Detrick, R. S., and G. M. Purdy, The crustal structure of the Kane Fracture Zone from seismic refraction studies, *J. Geophys. Res.*, *85*, 3759–3777, 1980.

Detrick, R. S., P. J. Fox, K. Kastens, W. B. F. Ryan, L. Mayer, and J. A. Karson, A Sea Beam survey of the Kane Fracture Zone and the adjacent Mid-Atlantic Ridge rift valley (abstract), *Eos Trans. AGU*, *65*, 1006, 1984.

Hanks, T. C., and M. Wyss, The use of body-wave spectra in the determination of seismic-source parameters, *Bull. Seismol. Soc. Am.*, *62*, 561–589, 1972.

Huang, P. Y., S. C. Solomon, E. A. Bergman, and J. L. Nabelek, Focal depths and mechanisms of Mid-Atlantic Ridge earthquakes from body waveform inversion, *J. Geophys. Res.*, *91*, 579–598, 1986.

Jackson, D. D., Interpretation of inaccurate, insufficient and inconsistent data, *Geophys. J. R. Astron. Soc.*, *28*, 97–110, 1972.

Jackson, J., and D. McKenzie, The geometrical evolution of normal fault systems, *J. Struct. Geol.*, *5*, 471–482, 1983.

Jordan, T. H., and K. A. Sverdrup, Teleseismic location techniques and their application to earthquake clusters in the south-central Pacific, *Bull. Seismol. Soc. Am.*, *71*, 1105–1130, 1981.

Karson, J. A., et al., Along-axis variations in seafloor spreading in the MARK area, *Nature*, *328*, 681–685, 1987.

Klein, F. W., Hypocenter location program HYPOINVERSE, 1, User's guide to versions 1, 2, 3, 4, *U.S. Geol. Surv. Open File Rep.*, *78-694*, 103 pp., 1978.

Koelsch, D. E., and G. M. Purdy, An ocean bottom hydrophone instrument for seismic refraction experiments in the deep ocean, *Mar. Geophys. Res.*, *4*, 115–125, 1979.

Kong, L., W. B. F. Ryan, L. A. Mayer, R. S. Detrick, P. J. Fox, and K. Manchester, Bare-rock drill sites, O. D. P. legs 106 and 109: Evidence for hydrothermal activity at 23°N on the Mid-Atlantic Ridge (abstract), *Eos Trans. AGU*, *66*, 936, 1985.

Kozlovsky, Y. A., Kola super-deep: Interim results and prospects, *Episodes*, *1982*(4), 9–11, 1982.

Langmuir, C. H., J. F. Bender, and R. Batiza, Petrological and tectonic segmentation of the East Pacific Rise, 5°30′–14°30′N, *Nature*, *322*, 422–429, 1986.

Lee, W. H. K., and S. W. Stewart, *Principles and Applications of Microearthquake Networks*, 293 pp., Academic, San Diego, Calif., 1981.

Lilwall, R. C., Fault mechanisms and sub-crustal seismic velocities on the Mid-Atlantic Ridge, *Geophys. J. R. Astron. Soc.*, *60*, 245–262, 1980.

Macdonald, K. C., and B. P. Luyendyk, Deep-tow studies of the structure of the Mid-Atlantic Ridge crest near lat 37°N, *Geol. Soc. Am. Bull.*, *88*, 621–636, 1977.

Macdonald, K. C., J.-C. Sempere, and P. J. Fox, East Pacific Rise from Siqueiros to Orozco fracture zones: Along-strike continuity of axial neovolcanic zone and structure and evolution of overlapping spreading centers, *J. Geophys. Res.*, *89*, 6049–6069, 1984.

Madariaga, R., Dynamics of an expanding circular fault, *Bull. Seismol. Soc. Am.*, *66*, 639–666, 1976.

Mayer, L. A., W. B. F. Ryan, L. Kong, and K. Manchester, Structure and tectonics of the Mid-Atlantic Ridge south of the Kane Fracture Zone based on Sea Marc I and Sea Beam site surveys (abstract), *Eos Trans. AGU*, *66*, 1092, 1985.

Minster, J. B., and T. H. Jordan, Present-day plate motions, *J. Geophys. Res.*, *83*, 5331–5354, 1978.

Ocean Drilling Program Leg 106 Scientific Party, Drilling the Snake Pit hydrothermal sulfide deposit on the Mid-Atlantic Ridge, lat 23°22′N, *Geology*, *14*, 1004–1007, 1986.

Ocean Drilling Program Leg 109 Scientific Party, Coring the crust and mantle, *Nature*, *323*, 482–483, 1986.

Pavlis, G. L., and J. R. Booker, The mixed discrete-continuous inverse problem: Application to the simultaneous determination of earthquake hypocenters and velocity structure, *J. Geophys. Res.*, *85*, 4801–4810, 1980.

Pereyra, V., W. H. K. Lee, and H. B. Keller, Solving two-point seismic-ray tracing problems in a heterogeneous medium, part 1, A general adaptive finite difference method, *Bull. Seismol. Soc. Am.*, *70*, 79–99, 1980.

Purdy, G. M., The correction for the travel time effects of seafloor topography in the interpretation of marine seismic data, *J. Geophys. Res.*, *87*, 8389–8396, 1982.

Purdy, G. M., and R. S. Detrick, The crustal structure of the Mid-Atlantic Ridge at 23°N from seismic refraction studies, *J. Geophys. Res.*, *91*, 3739–3762, 1986.

Schouten, H., and K. D. Klitgord, The memory of the accreting plate boundary and the continuity of fracture zones, *Earth Planet. Sci. Lett.*, *59*, 255–266, 1982.

Schouten, H., K. D. Klitgord, and J. A. Whitehead, Segmentation of mid-ocean ridges, *Nature*, *317*, 225–229, 1985.

Sutton, G. H., F. K. Duennebier, and B. Iwatake, Coupling of ocean bottom seismometers to soft bottoms, *Mar. Geophys. Res.*, *5*, 35–51, 1981.

Thomson, D. J., Spectrum estimation techniques for characterization and development of WT4 waveguide, 1, *Bell Syst. Tech. J.*, *56*, 1769–1815, 1977.

Thurber, C. H., Earth structure and earthquake locations in the Coyote Lake area, central California, Ph.D. thesis, 332 pp., Mass. Inst. of Technol., Cambridge, 1981.

Thurber, C. H., Earthquake locations and three-dimensional crustal structure in the Coyote Lake area, central California, *J. Geophys. Res.*, *88*, 8226–8236, 1983.

Toomey, D. R., S. C. Solomon, G. M. Purdy, and M. H. Murray,

Microearthquakes beneath the median valley of the Mid-Atlantic ridge near 23°N: Hypocenters and focal mechanisms, *J. Geophys. Res.*, *90*, 5443–5458, 1985.

Tréhu, A. M., and S. C. Solomon, Coupling parameters of the MIT OBS at two nearshore sites, *Mar. Geophys. Res.*, *5*, 69–78, 1981.

Tréhu, A. M., and S. C. Solomon, Earthquakes in the Orozco transform zone: Seismicity, source mechanisms, and tectonics, *J. Geophys. Res.*, *88*, 8203–8225, 1983.

Urick, R. J., *Principles of Underwater Sound*, 2nd ed., 384 pp., McGraw-Hill, New York, 1975.

Whitehead, J. A., H. J. B. Dick, and H. Schouten, A mechanism for magmatic accretion under spreading centres, *Nature*, *312*, 146–148, 1984.

Wiggins, R. A., The general linear inverse problem: Implication of surface waves and free oscillations for Earth structure, *Rev. Geophys.*, *10*, 251–285, 1972.

G. M. Purdy, Department of Geology and Geophysics, Woods Hole Oceanographic Institution, Woods Hole, MA 02543.

S. C. Solomon and D. R. Toomey, Department of Earth, Atmospheric and Planetary Sciences, Room 54-512, Massachusetts Institute of Technology, Cambridge, MA 02139.

(Received July 23, 1987;
revised April 1, 1988;
accepted April 8, 1988.)